TWO TYPE IA SUPERNOVAE AT REDSHIFT ~2 : IMPROVED CLASSIFICATION AND REDSHIFT DETERMINATION WITH MEDIUM-BAND INFRARED IMAGING

Steven A. Rodney[1,2,3], Adam G. Riess[1,4], Daniel M. Scolnic[5], David O. Jones[1], Shoubaneh Hemmati[6], Alberto Molino[7,8], Curtis McCully[9,10], Bahram Mobasher[6], Louis-Gregory Strolger[4,11], Or Graur[12,13], Brian Hayden[14,15], and Stefano Casertano[4]

Draft version August 14, 2015

ABSTRACT

We present two supernovae (SNe) discovered with the *Hubble Space Telescope* (HST) in the Cosmic Assembly Near-infrared Deep Extragalactic Legacy Survey (CANDELS), an HST multi-cycle treasury program. We classify both objects as Type Ia SNe and find redshifts of $z = 1.80 \pm 0.02$ and $2.26^{+0.02}_{-0.10}$, the latter of which is the highest redshift Type Ia SN yet seen. Using light curve fitting we determine luminosity distances and find that both objects are consistent with a standard ΛCDM cosmological model. These SNe were observed using the HST Wide Field Camera 3 infrared detector (WFC3-IR), with imaging in both wide- and medium-band filters. We demonstrate that the classification and redshift estimates are significantly improved by the inclusion of single-epoch medium-band observations. This medium-band imaging approximates a very low resolution spectrum ($\lambda/\Delta\lambda \lesssim 100$) which can isolate broad spectral absorption features that differentiate Type Ia SNe from their most common core collapse cousins. This medium-band method is also insensitive to dust extinction and (unlike grism spectroscopy) it is not affected by contamination from the SN host galaxy or other nearby sources. As such, it can provide a more efficient – though less precise – alternative to IR spectroscopy for high-z SNe.

Subject headings: cosmology: observations, methods: observational, supernovae: general

1. INTRODUCTION

Type Ia supernovae (SNe) at redshifts $z > 1$ are a valuable tool for measuring the expansion history of the universe and for testing models of Type Ia SN progenitor systems. Measurements of the Type Ia SN rate at $z > 1$ have been used to constrain Type Ia SN progenitor models through the delay time distribution test (Poznanski et al. 2007; Graur et al. 2011; Dahlen et al. 2004; Strolger

srodney@sc.edu
[1] Department of Physics and Astronomy, The Johns Hopkins University, 3400 N. Charles St., Baltimore, MD 21218, USA
[2] Department of Physics and Astronomy, University of South Carolina, 712 Main St., Columbia, SC 29208, USA
[3] Hubble Fellow
[4] Space Telescope Science Institute, 3700 San Martin Dr., Baltimore, MD 21218, USA
[5] Department of Physics, The University of Chicago, Chicago, IL 60637, USA
[6] Department of Physics and Astronomy, University of California, Riverside, CA 92521, USA
[7] Instituto de Astrofísica de Andalucía (CSIC), E-18080 Granada, Spain
[8] Instituto de Astronomia, Geofísica e Ciências Atmosféricas, Universidade de São Paulo, Cidade Universitária, 05508-090, São Paulo, Brazil
[9] Las Cumbres Observatory Global Telescope Network, 6740 Cortona Dr., Suite 102, Goleta, California 93117, USA
[10] Department of Physics, University of California, Santa Barbara, CA 93106-9530, USA
[11] Department of Physics, Western Kentucky University, Bowling Green, KY 42101, USA
[12] Center for Cosmology and Particle Physics, New York University, New York, NY 10003, USA
[13] Department of Astrophysics, American Museum of Natural History, Central Park West and 79th Street, New York, NY 10024, USA
[14] Department of Physics, University of Notre Dame, Notre Dame, IN 46556, USA
[15] Lawrence Berkeley National Laboratory, Berkeley, CA 94720, USA

& Riess 2006; Dahlen et al. 2008) and recent extensions of the sample to $z \sim 2$ are providing unique leverage on the fraction of Type Ia SN progenitors that explode promptly after formation (Graur et al. 2014; Rodney et al. 2014, hereafter R14).

A subset of these high-z Type Ia SNe with well sampled light curves has been used to extend luminosity distance measurements into an era when the universe was decelerating. A notable early example is SN 1997ff (Gilliland et al. 1999; Riess et al. 2001), which held the title of the farthest known Type Ia SN for over a decade (until Jones et al. 2013). By reaching into the early universe, SN 1997ff and other high-z Type Ia SNe provided a valuable check against systematic effects that could mimic dark energy signatures at lower z (Riess et al. 2000, 2001; Tonry et al. 2003; Riess et al. 2004b). As the sample of high-z Type Ia SNe has grown, it has also delivered limits on the evolution of the equation of state of the universe over cosmic time (Riess et al. 2007; Suzuki et al. 2012).

Discovering Type Ia SNe and measuring their rest-frame optical light curves at $z > 1$ requires deep infrared imaging. This imaging data alone has been widely used for measuring Type Ia SN rates to test SN progenitor models, aided by an increasingly rigorous suite of photometric classification software (e.g., Poznanski et al. 2007; Rodney & Tonry 2009; Kessler et al. 2010; Sako et al. 2011).

However, SN cosmology is still almost exclusively limited to samples with spectroscopic classifications (e.g., Rest et al. 2014, Betoule et al. 2014; but see Campbell et al. 2013). Spectroscopic observations of SNe in the range $1 < z < 1.5$ with ground-based telescopes are feasible, but very challenging (e.g., Lidman et al. 2005; Morokuma et al. 2010). The task is more man-

ageable from space, and slitless grism spectroscopy with the Hubble Space Telescope (HST) Advanced Camera for Surveys (ACS) has been used to successfully classify 16 Type Ia SNe in this redshift range (Riess et al. 2004a,b; Riess et al. 2007; Graur et al. 2014, R14). However, as SNe discoveries are pushed to redshifts $z > 1.5$, such direct spectroscopic SN classifications become increasingly costly and less definitive (Rodney et al. 2012; Rubin et al. 2013; Jones et al. 2013).

In cases where the SN spectrum cannot independently define the SN class and redshift, we may make use of photometric classifications and host galaxy redshifts. However, biases in the derived redshift and distance are more likely in such cases, due to errors in host galaxy association or when a spectroscopic redshift for the host galaxy is unavailable. Host galaxy redshifts are especially problematic for SNe in the so-called redshift desert $(1.4 < z < 2.5)$, which is precisely the current frontier for high-z SN searches with HST. Newer infrared spectrometers on 8-meter class telescopes are able to define precise spectroscopic redshifts for some SN host galaxies in this redshift range, but it remains a challenging endeavor (e.g., Amanullah et al. 2011; Frederiksen et al. 2012, 2014). These biases can also be reduced – though not wholly eliminated – by designing surveys around galaxy clusters, where SNe appearing in early-type cluster member galaxies have less ambiguity in both class and redshift (Dawson et al. 2009).

In Section 2 we present an alternative approach for determining the classification and redshift of SNe at $z > 1.4$. This method builds on the "SN Cross Correlation" imaging technique of Scolnic et al. (2009, hereafter S09), extending it to higher redshifts by using medium-band imaging from the HST WFC3-IR detector. Unlike photometric constraints from pure broad-band imaging, this approach is insensitive to reddening, and is able to test for specific individual absorption features in the SN spectral energy distribution (SED). This medium-band method is more efficient than slitless spectroscopy with an HST grism, and is also largely unaffected by contamination from nearby bright sources.

Section 3 describes the discovery and observation of two Type Ia SNe at $z \sim 2$, found in the SN search component of the Cosmic Assembly Near-infrared Deep Extragalactic Legacy Survey (CANDELS, Koekemoer et al. 2011; Grogin et al. 2011). In Sections 4 and 5 we apply the HST medium-band imaging technique to help define the classification and redshift of each SN. A third high-redshift SN, classified as a Core Collapse SN (CC SN), is presented in the Appendix. The value of the medium-band imaging method is examined in Section 6, and in Section 7 we put these SN discoveries into the context of current Type Ia SN cosmology. Finally, our results and conclusions are briefly summarized in Section 8.

2. PSEUDO-SPECTROSCOPY WITH MEDIUM BAND FILTERS

The SED of a Type Ia SN near maximum light is dominated by a series of broad absorption features interspersed with pseudo-continuum peaks, creating a roughly sinusoidal pattern over the rest-frame wavelength range 3500-6500 Å (e.g., Filippenko 1997). S09 introduced the specialized SuperNovA Cross Correlation (SNACC) filters, a set of custom optical filters designed to take ad-
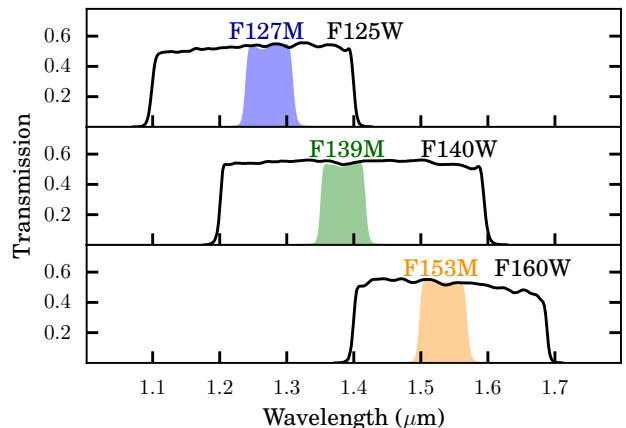

Figure 1. The three primary medium band filters for the HST WFC3-IR camera, and their complementary wide band filters. The transmission function of each medium-band filter is shown as a filled curve, and the accompanying wide-band filter as a solid black line. These three pairs define the medium-minus-wide pseudo-colors used throughout this work.

vantage of this crudely periodic SED shape. Each filter has 3 pass-bands ("teeth") that approximately match the width and spacing of the SNIa spectral features. S09 showed that SNACC filter observations combined with traditional broad band imaging from the Pan-STARRS1 SN survey could deliver a Type Ia SN sample with 98% purity and redshift precision of $\sigma_z = 0.01$, all with an efficiency up to $\sim$30 times better than traditional spectroscopic follow-up. In addition to the efficiency gains, this comb filter approach is largely insensitive to dust extinction, and can easily employ image subtraction techniques to minimize contamination of the SN signal by the underlying host galaxy light.

The SNACC filters employed by S09 were optimized for SNe in the redshift range $0.2 < z < 0.8$, in order to target SNe discovered in ground-based surveys. To extend this technique to higher redshift SNe, we must turn to infrared (IR) wavelengths. The HST WFC3-IR camera includes a set of medium-band filters (F098M,F127M,F139M,F153M) which can collectively approximate the teeth of the SNACC comb filters. These four medium-band filters on the WFC3-IR detector were designed as grism reference bands or to pick out molecular absorption features in extrasolar planets (e.g., H_2O, CH_4, NH_3). The F098M filter spans 157 nm, while the three redder bands have a width of $\sim$ 65 nm. By comparison, the wide-band IR filters such as F125W (J) and F160W (H) cover $\sim$ 275 nm each. As shown in Figure 1, each of the medium-band filters has a corresponding wide-band filter that completely contains the medium-band filter wavelengths. Throughout this work we use *medium-minus-wide* pseudo-colors, subtracting the magnitude of a source in the wide band from the medium-band magnitude (e.g., F127M-F125W). This is consistent with the convention set in S09 for the SNACC filters.

The spectral absorption features of Type Ia SNe span roughly 30 nm in the rest frame, so for a high-redshift SN at $1.5 < z < 2.5$ the observer finds them broadened to widths of $75 - 105$ nm. As shown on the left side of Figure 2, this means that the medium-band filter widths are
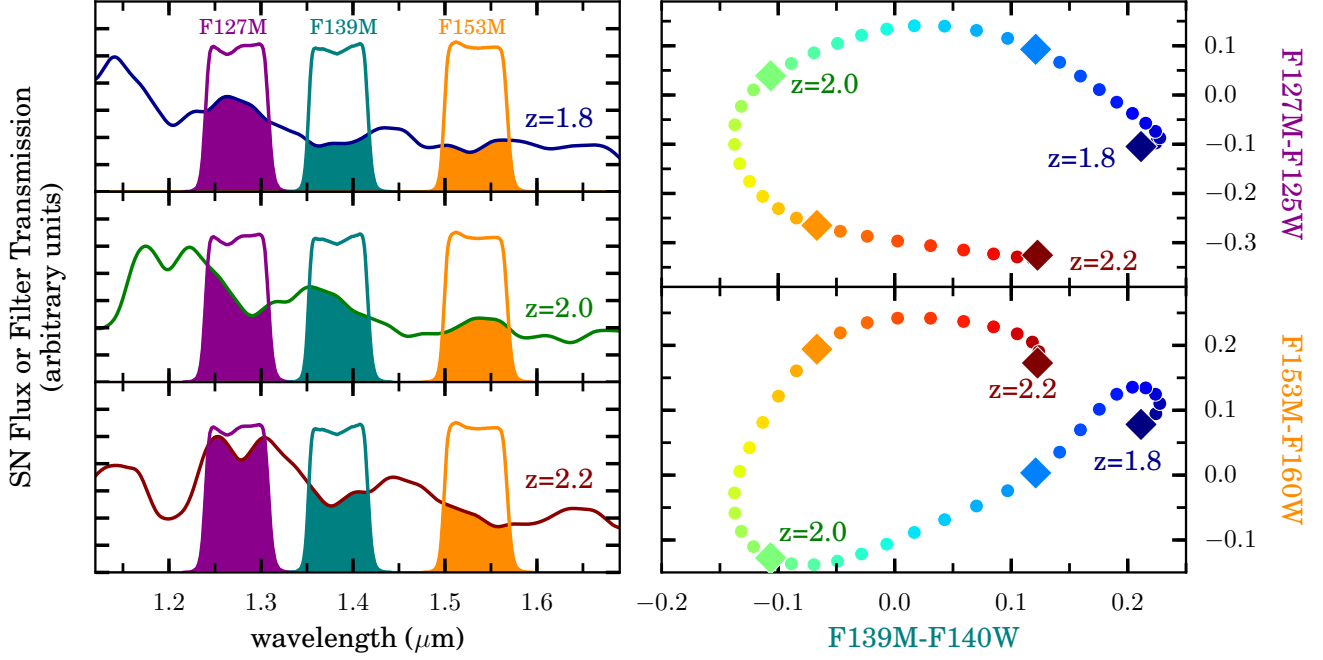
Figure 2. Demonstration of the method for determining a Type Ia SN redshift from medium−wide band pseudo-colors. Three panels at left show the SED of a template Type Ia SN (Hsiao et al. 2007) at peak brightness with no extinction. From top to bottom these panels show the SED at redshifts of 1.8, 2.0, and 2.2. Overlaid on each SED are the transmission curves for the WFC3-IR medium band filters. As the redshift increases, broad absorption features are moved in and out of the band passes, causing cyclic changes in the observed flux through each band, relative to the encompassing broad bands (not shown). In two panels at right we plot the medium−wide pseudo-colors, mapping the results of changing the redshift from $z = 1.8$ to 2.2.

well suited for isolating the spectral features characteristic of Type Ia SNe in this redshift range. Observations with traditional wide-band filters must accompany each medium-band observation in order to provide a continuum reference point. The medium-band pseudo-colors (e.g. F139M-F140W) indicate whether the medium band filter intersects an absorption feature (resulting in a more positive pseudo-color) or a brighter continuum region (more negative pseudo-color). As redshift increases, the absorption features migrate in and out of the medium band regions, so pseudo-colors move from positive to negative and back again. In a plot comparing two pseudo-colors, as shown in Figure 2, a Type Ia SN will trace out a circle as it is moved through redshift space. For redshifts $1.5 < z < 2.5$, measuring three of these pseudo-colors near peak brightness to better than 0.1 mags can yield a redshift estimate with precision approaching 2% in $\Delta z/(1 + z)$, comparable to the best available photometric redshifts from galaxy SED fitting (Hildebrandt et al. 2010; Dahlen et al. 2013).

The medium-band pseudo-colors are also useful for classification of SNe at $z > 1.5$. The spectra of core collapse SNe (CC SNe) do not have the same semi-periodic absorption features as in Type Ia SNe. CC SN SEDs are also much more heterogeneous, so the space that they populate in a pseudo-color vs pseudo-color plot is not a circle, but an amorphous cloud. As shown in Figure 3, the most common sub-class of CC SNe (Type II) is centered near the origin of the pseudo-color space, so the location of a SN in this space can be a useful indicator of its class.

The use of medium-band pseudo-colors has several

qualitative features that make it attractive for SN classification. First, by using relative flux instead of absolute flux measures (i.e. colors instead of magnitudes), this method does not require any assumptions about the underlying cosmology or luminosity function of the high-redshift SN populations. Second, the wide- and medium-band filters in each color pair occupy the same portion of the SED, so this method is insensitive to the overall color of the SED. Therefore, as shown in Figure 4, the classification is largely unaffected by SN host galaxy extinction: medium−wide pseudo-colors are changed by less than 0.01 mag per 1 mag of extinction.

Medium-band imaging is also substantially more efficient than spectroscopy. As shown in Jones et al. (2013), observing a typical Type Ia SN at $z > 1.5$ with the WFC3-IR G141 grism requires at least 10 HST orbits (25 ksec) to get sufficient signal-to-noise (S/N) for discriminating a Type Ia SN spectrum from that of a Type II SN. To rule out possible mis-classification of Type Ib or Ic SNe as Type Ia SN requires considerably more: as many as $\sim$70 orbits at $z \sim 2$. HST grism observations are also often limited by systematic uncertainties due to contamination from the SN host galaxy and other nearby sources that overlap the SN spectrum. By contrast, in this medium band imaging method we use spectral elements that have $\sim$15% better total throughput at any given wavelength than the G141 grism.

With medium-band imaging we can also utilize existing wide-band template images (already needed for measuring the wide-band light curve) to subtract out contaminating background light very cleanly. That is, we get the advantages of host galaxy subtraction without
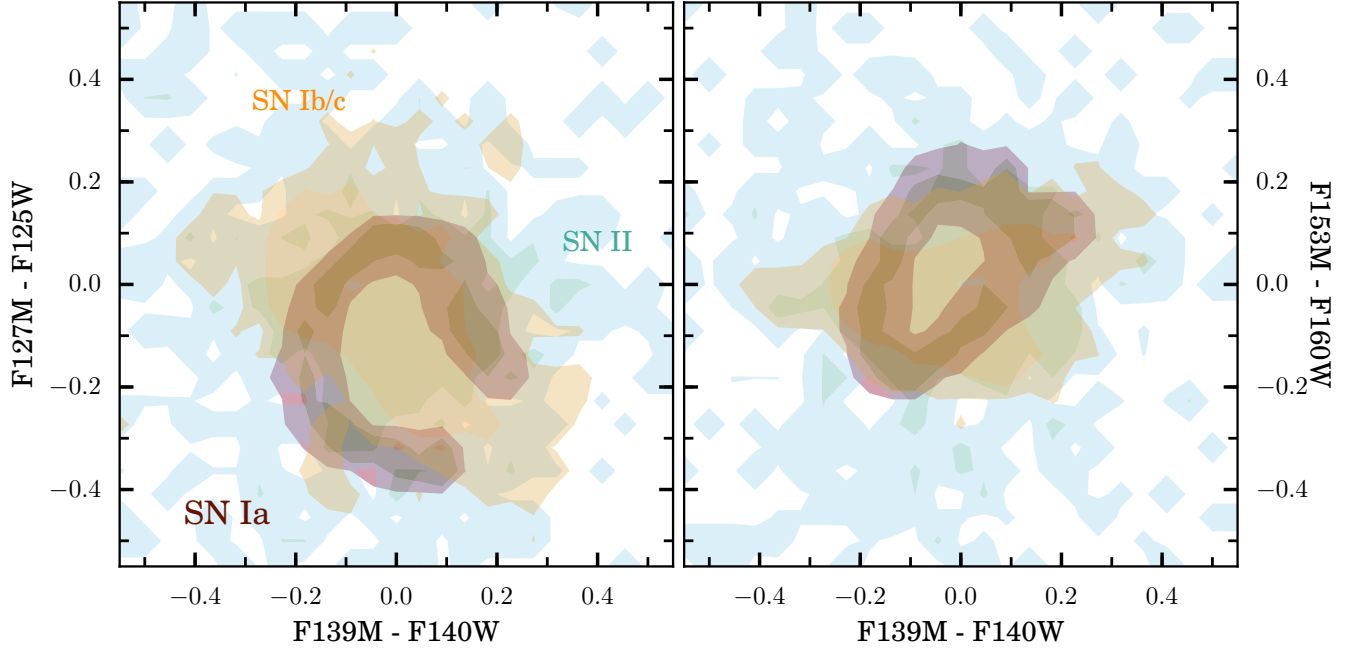
Figure 3. Demonstration of the segregation of SN populations in *medium−wide* pseudo-color space. Contours show the colors measured from 5000 simulated SN of each class, evenly sampling the redshift range z=[1.8,2.2], with Monte Carlo sampling of light curve templates and parameters – including luminosity and host galaxy extinction – following R14. Solid line contours enclose 68% of the population and filled contours enclose 95% for each class, with red for Type Ia SNe, green for Type II, and yellow for Type Ib/c. The separation of the Type Ia contours from the CC SN sub-types means that these pseudo-color plots can be useful aids for classifying observed high-z SNe.
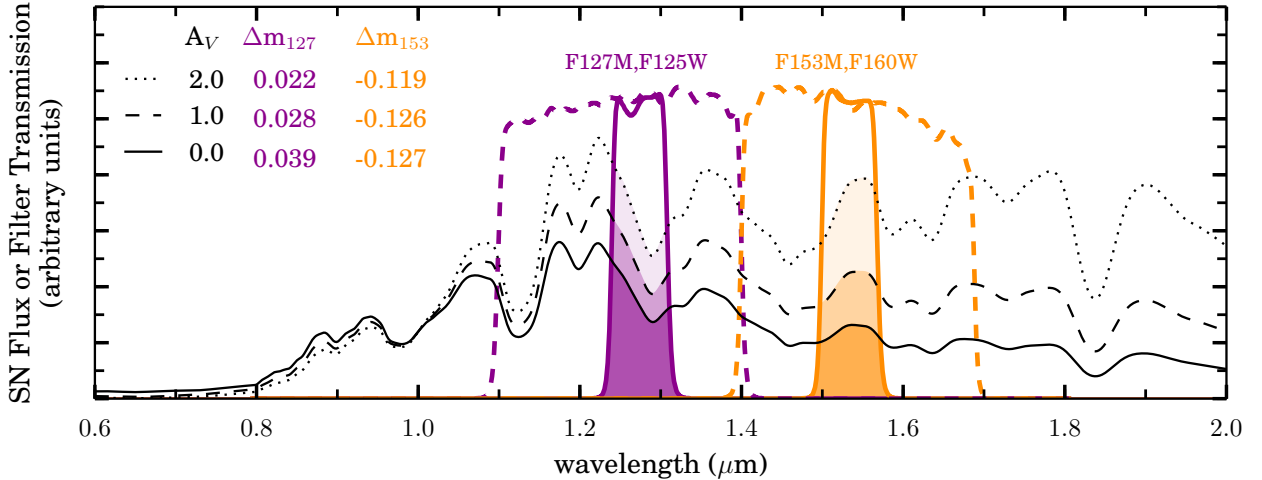
Figure 4. The medium-band pseudo-colors are largely insensitive to extinction. Black curves show the SED of a Type Ia SN template at z=2.0 and peak brightness (Hsiao et al. 2007). Three curves show the effect of host galaxy extinctions from A_V=0.0 to 2.0, using an extinction law with R_V=3.1 (Cardelli et al. 1989; O'Donnell 1994). The SEDs have been normalized at 1 μm. Although the overall SED is substantially reddened, the pseudo-colors change by only ∼2%, as given in the legend in AB mag colors for F127M-F125W and F153M-F160W.

requiring an additional post-SN epoch of medium-band imaging. To do so, we make the justifiable assumption that the host galaxy does not have any broad spectral features that match the width of the medium band filters. With that assumption, we can create a SN-free medium-band template image by simply scaling the flux of the wide-band template using a ratio of the medium- and wide-band filter transmissions.

In the following sections we will examine two examples from the CANDELS SN program where medium-band imaging is employed at a total cost of only 5-10 HST orbits ($\sim$10-20 ksec) across all medium-band filters.

3. SN DISCOVERY AND OBSERVATIONS

We now turn from the theory of this technique to the actual practice, as applied to a pair of SNe discovered in the CANDELS multi-cycle treasury program on HST. The SN component of the CANDELS program was operated jointly alongside the Cluster Lensing And Supernova Survey with Hubble (CLASH, Postman et al. 2012), and the two programs together discovered and characterized $\sim$100 SNe over 3 years (Rodney et al. 2012, Jones et al. 2013, R14, Graur et al. 2014, Patel et al. 2014) Follow-up observations with HST were executed through the CANDELS/CLASH SN program (PI:Riess, HST Program ID:12099). The SNe in this work were first presented in R14, where we measured the volumetric Type Ia SN rate as a function of redshift from the full CANDELS SN sample.

SN GND13Sto (Section 4) and GND12Col (Section 5) were discovered in IR imaging on the CANDELS GOODS-S and GOODS-N fields, respectively. In both cases these SN were immediately identified as likely high-redshift sources based on preliminary host galaxy photo-z measurements and their observed brightnesses. These SNe were also initially classified as Type Ia candidates, based on their rest-frame UV-optical color deficit (as in Riess et al. 2004a; Rodney et al. 2012; Jones et al. 2013). No definitive spectroscopic redshifts were available for either of these objects at the time of discovery, and they were both quite faint, so spectroscopic follow-up with the HST grisms was deemed too risky. Instead, we applied the medium band imaging technique, described in detail below.

Table 1 summarizes the discovery dates, coordinates, and host galaxy redshifts of all three objects. In R14 we provided classifications and redshifts based only on the broad-band SN light curves and host information. Here we will refine both class and redshift with the addition of medium-band IR data and improved photometry. We also extend the analysis to determine luminosity distances for the two objects classified as Type Ia, in order to compare them to the larger SN samples at $z < 1$.

3.1. Data Processing and Photometry

For each SN, we collected from the HST archive all available imaging from the Wide Field Camera 3 (WFC3-IR and WFC3-UVIS) and the Advanced Camera for Surveys Wide Field Camera (ACS-WFC). These data were then processed using a custom pipeline `sndrizpipe`[16] that sorts the HST images into epochs, then combines

and registers them using the `DrizzlePac` software from the Space Telescope Science Institute (STScI) (Fruchter et al. 2010). For each filter, a template image was constructed from all epochs that were at least 30 days before the SN appeared or 90 days after the last 3σ detection. The template images were directly subtracted from every epoch containing SN light to get difference images. It was not necessary to convolve with the point spread function (PSF) for optimal subtraction (Alard & Lupton 1998), owing to the excellent stability of the HST PSF.

Fluxes and AB magnitudes for GND13Sto and GND12Col are given in Tables 2 and 3, respectively. In the WFC3-IR difference images we measured the SN flux using PSF-fitting photometry, with a PSF model constructed from the G2V standard star P330E. Flux uncertainties were estimated by separately planting 10,000 synthetic SNe into the difference image and fitting a Gaussian to the distribution of recovered fluxes.

For both of these SNe we have no detections above 3σ in the ACS-WFC or WFC3-UVIS imaging. In those bluer bands (corresponding to the rest-frame UV for these SNe) we used the `hstphot` package[17] to collect aperture photometry in a $0.4''$ aperture, with zero points and aperture corrections as published by STScI.[18]

3.2. Galaxy Photometry, Host Association and SED Fitting

To evaluate galaxies in the vicinity of our SNe as candidate hosts and potential gravitational lenses, we use a photometry catalog including data from all available optical and IR bands. All photometry was collected using SExtractor (Bertin & Arnouts 1996) for source detection and TFIT (Laidler et al. 2007) for matched-aperture photometry, as detailed in Guo et al. (2013) and Fontana et al. (2014). For CANDELS data where the SN was detected (i.e. the WFC3 IR bands) we measured photometry from the SN-free template images instead of the full-depth CANDELS mosaics.

To determine which of the nearby galaxies (if any) could plausibly be associated with each SN, we follow the procedure of Sullivan et al. (2006), which is designed to infer the most likely SN host galaxy based on angular separation and galaxy size. Using SExtractor on the F160W images, we define a Kron (1980) ellipse centered at position x_{gal}, y_{gal}, with semimajor axis r_A, semiminor axis r_B and position angle θ. The separation from the galaxy to any given position (x, y) is quantified by the elliptical radius, R, defined as

$$R^2 = C_{xx}x_r^2 + C_{yy}y_r^2 + C_{xy}x_ry_r, \qquad (1)$$

where $x_r = x - x_{gal}$, $y_r = y - y_{gal}$, $C_{xx} = \cos^2(\theta)/r_A^2 + \sin^2(\theta)/r_B^2$, $C_{yy} = \sin^2(\theta)/r_A^2 + \cos^2(\theta)/r_B^2$, and $C_{xy} = 2\cos(\theta)\sin(\theta)(1/r_A^2 - 1/r_B^2)$. An ellipse with radius $R = 2.5$ will typically contain $\sim$90% of the object's light (Infante 1987; Graham & Driver 2005). For consideration as a possible SN host galaxy, Sullivan et al. (2006) used the requirement that the SN position must lie within an

---

[16] `sndrizpipe` v1.2 https://github.com/srodney/sndrizpipe

[17] https://github.com/srodney/hstphot; based on a translation of the IDL AstroLib photometry routines (Landsman 1993) into Python.

[18] For WFC3: http://www.stsci.edu/hst/wfc3/phot_zp_lbn; for ACS: http://www.stsci.edu/hst/acs/analysis/zeropoints

Table 1
SN Discovery Data

Supernova	SN Coordinates[a]	Host Galaxy Coordinates[b]	Discovery Date	Host Redshift	Host z Source[c]
GND13Sto	12:37:16.77 +62:16:41.4	12:37:16.59 +62:16:43.4	UT 2013 Jun14.5	1.80 ± 0.02	Spitzer IRS
GND12Col	12:36:37.58 +62:18:33.0	12:36:37.51 +62:18:32.6	UT 2012 May27.3	2.26 ± 0.09	CANDELS phot-z
GSD11Bus[d]	03:32:42.78 −27:48:07.1	03:32:42.78 −27:48:07.1	UT 2011 Aug05.8	$1.15^{+0.19}_{-0.38}$	CANDELS phot-z

[a] R.A. and Decl. in J2000 ICRS coordinates.
[b] The center of the SN host galaxy in J2000 ICRS coordinates. For GND13Sto we give coordinates of the most likely host: stoneA.
[c] Primary source for host galaxy redshift, independent of the SN photometry. See text for details.
[d] SN GSD11Bus is discussed in the appendix.

Table 2
GND13Sto Photometry

Obs. Date (MJD)	Filter	Exp. Time (sec)	Flux (counts/sec)	Flux Err (counts/sec)	AB Mag[a]	Mag Err	AB Zero Point	ΔZP[b] (Vega-AB)
56403.4	F350LP	434	0.0236	0.1375	>27.9	$\cdots$	26.949	-0.156
56457.5	F350LP	434	0.1084	0.1430	>27.9	$\cdots$	26.949	-0.156
56490.6	F350LP	544	0.1271	0.1292	>28.0	$\cdots$	26.949	-0.156
56513.4	F350LP	434	-0.0748	0.1548	>27.8	$\cdots$	26.949	-0.156
56406.7	F814W	6708	0.0864	0.0675	28.606	0.849	25.947	-0.424
56458.3	F814W	2236	0.1512	0.0876	27.998	0.629	25.947	-0.424
56410.7	F850LP	1946	-0.1063	0.0917	>26.3	$\cdots$	24.857	-0.519
56403.4	F125W	1156	0.2437	0.1155	27.763	0.515	26.230	-0.901
56457.5	F125W	1156	1.1137	0.1564	26.113	0.152	26.230	-0.901
56467.9	F125W	1256	2.1157	0.1614	25.416	0.083	26.230	-0.901
56490.6	F125W	1006	2.3250	0.1907	25.314	0.089	26.230	-0.901
56513.4	F125W	1156	1.2606	0.1651	25.979	0.142	26.230	-0.901
56531.1	F125W	503	0.4965	0.1907	26.990	0.417	26.230	-0.901
56474.4	F139M	5023	0.4202	0.0791	25.420	0.204	24.479	-1.076
56474.5	F140W	1356	2.7573	0.3110	25.351	0.122	26.452	-1.076
56474.9	F153M	5023	0.4106	0.0621	25.429	0.164	24.463	-1.254
56403.4	F160W	1206	0.1636	0.1493	27.911	0.991	25.946	-1.251
56457.5	F160W	1206	1.0590	0.1611	25.884	0.165	25.946	-1.251
56467.9	F160W	1206	1.2366	0.1543	25.715	0.136	25.946	-1.251
56474.5	F160W	1206	1.9397	0.1501	25.227	0.084	25.946	-1.251
56490.6	F160W	1006	1.5039	0.1728	25.503	0.125	25.946	-1.251
56513.4	F160W	1206	1.3238	0.1740	25.641	0.143	25.946	-1.251
56531.1	F160W	1609	0.9151	0.1628	26.042	0.193	25.946	-1.251
56551.2	F160W	2462	0.7125	0.1277	26.314	0.195	25.946	-1.251

[a] For flux values of less than 1σ significance we report the magnitude as a 3σ upper limit
[b] Zero point difference: the magnitude shift for conversion from AB to Vega magnitude units.

ellipse with $R = 5$, and found that ~93% of SNe in the Supernova Legacy Survey (SNLS) had at least one detected host candidate meeting that criterion. Ellipse parameters for the nearest galaxies to each SN are reported in Table 4. Note that this approach does not make use of any redshift information about the SN or the nearby galaxies. In the following sections we will also bring to bear the available spectroscopic and photometric redshift evidence.

To determine the photo-z and estimate physical parameters, we fit each galaxy's SED using the LePhare code for SED matching via χ^2 minimization (Arnouts et al. 1999; Ilbert et al. 2006). We employ a template library based on the PICKLES stellar spectra (Pickles 1998), the LePhare quasar templates, and the BC03 models for galaxy SEDs (Bruzual & Charlot 2003). A Chabrier initial mass function is assumed (Chabrier 2003). Further details of the SED-fitting process are given in Hemmati et al. (2014). Note, however, that

in Hemmati et al. (2014) each galaxy is subdivided to kpc-scale resolution. For this work we use the integrated light of the entire galaxy. Table 4 reports the results from this SED fitting, giving the photometric redshift, best-fit galaxy type, and an estimate of the total stellar mass. We find the photometric redshifts are in very good agreement with the few available spectroscopic redshifts. In those cases where a spectroscopic redshift exists, the redshift is fixed at that value for determination of the best-fit galaxy type and stellar mass.

4. GND13Sto : SN STONE

4.1. *GND13Sto Host Galaxy*

The first of our two high-z Type Ia SN candidates is GND13Sto, [19] discovered in exposures taken on 14 June

[19] Nicknamed "SN Stone," after Thomas Stone, a signatory of the United States Declaration of Independence as a delegate from Maryland

Table 3
GND12Col Photometry

Obs. Date (MJD)	Filter	Exp. Time (sec)	Flux (counts/sec)	Flux Err (counts/sec)	AB Mag[a]	Mag Err	AB Zero Point	ΔZP[b] (Vega-AB)
56018.7	F350LP	434	0.2079	0.1657	28.654	0.865	26.949	-0.156
56074.3	F350LP	868	-0.2289	0.1649	>27.7	⋯	26.949	-0.156
56129.4	F350LP	434	-0.3159	0.2412	>27.3	⋯	26.949	-0.156
56145.5	F350LP	400	-0.0398	0.1953	>27.5	⋯	26.949	-0.156
56070.0	F606W	982	-0.0505	0.1123	>27.7	⋯	26.493	-0.086
56016.3	F814W	2536	0.1885	0.1006	27.759	0.580	25.947	-0.424
56074.6	F814W	3535	0.1318	0.0952	28.141	0.784	25.947	-0.424
56116.5	F814W	7072	-0.0889	0.0746	>27.6	⋯	25.947	-0.424
56128.4	F814W	6708	-0.0630	0.0834	>27.5	⋯	25.947	-0.424
56180.9	F814W	2236	-0.0433	0.1186	>27.1	⋯	25.947	-0.424
56200.2	F814W	2396	0.0735	0.0479	28.781	0.708	25.947	-0.424
56152.1	F850LP	1442	-0.0647	0.0746	>26.5	⋯	24.857	-0.519
56018.6	F125W	1156	-0.0049	0.0703	>27.9	⋯	26.230	-0.901
56074.3	F125W	1156	1.2037	0.1440	26.029	0.130	26.230	-0.901
56084.7	F125W	1206	1.1206	0.1487	26.106	0.144	26.230	-0.901
56103.2	F125W	1206	0.8749	0.1514	26.375	0.188	26.230	-0.901
56129.5	F125W	2309	0.2662	0.0990	27.667	0.404	26.230	-0.901
56145.6	F125W	2562	0.2219	0.1033	27.864	0.505	26.230	-0.901
56183.1	F125W	1156	-0.0035	0.0708	>27.9	⋯	26.230	-0.901
56242.0	F125W	1156	0.0000	0.0763	>27.8	⋯	26.230	-0.901
56297.7	F125W	1156	0.0140	0.0742	>27.9	⋯	26.230	-0.901
56084.8	F127M	7485	0.3853	0.0447	25.677	0.126	24.641	-0.961
56082.8	F139M	8291	0.3472	0.0527	25.628	0.165	24.479	-1.079
56083.1	F140W	1706	1.9370	0.1847	25.734	0.103	26.452	-1.076
56091.5	F140W	506	1.8524	0.2847	25.783	0.167	26.452	-1.076
56104.2	F140W	506	1.3515	0.2988	26.125	0.240	26.452	-1.076
56085.7	F153M	7485	0.2942	0.0543	25.791	0.201	24.463	-1.254
56018.6	F160W	1206	-0.0116	0.1823	>26.6	⋯	25.946	-1.251
56074.3	F160W	1206	1.3706	0.1727	25.604	0.137	25.946	-1.251
56084.7	F160W	1206	1.0138	0.1547	25.931	0.166	25.946	-1.251
56103.2	F160W	1256	0.9008	0.1550	26.059	0.187	25.946	-1.251
56129.4	F160W	2762	0.4049	0.1231	26.928	0.330	25.946	-1.251
56145.5	F160W	2009	0.5715	0.1500	26.553	0.285	25.946	-1.251
56183.1	F160W	1206	0.2813	0.1489	27.323	0.575	25.946	-1.251
56242.0	F160W	1206	0.0664	0.2891	>26.1	⋯	25.946	-1.251
56297.7	F160W	1206	-0.0234	0.2204	>26.4	⋯	25.946	-1.251

[a] For flux values of less than 1σ significance we report the magnitude as a 3σ upper limit
[b] Zero point difference: the magnitude shift for conversion from AB to Vega magnitude units.


Table 4
Kron Ellipse Parameters and Properties of Host Galaxy and Lens Candidates

ID	r_A ('')	r_B ('')	θ (deg)	R_{SN}	spec-z	photo-z[a]	$\log_{10}(M/M_\odot)$[b]	spec-z Ref.
colfaxA	0.34	0.25	0.0	1.6	⋯	$2.26^{+0.09}_{-0.09}$	$9.98^{+0.10}_{-0.06}$	⋯
colfaxB	0.64	0.46	89.4	4.4	0.9466 ± 0.0002	$0.95^{+0.14}_{-0.04}$	$9.87^{+0.17}_{-0.14}$	Cowie et al. 2004
stoneA	0.60	0.26	52.1	3.9	1.80 ± 0.02	$1.70^{+0.23}_{-0.13}$	$11.37^{+0.31}_{-0.12}$	Murphy et al. 2009
stoneB	0.59	0.41	76.8	5.0	⋯	$1.55^{+0.66}_{-0.22}$	$10.13^{+0.29}_{-0.25}$	⋯
stoneC	0.66	0.31	51.1	5.5	0.5572 ± 0.0002	$0.65^{+0.05}_{-0.07}$	$9.23^{+0.20}_{-0.24}$	Wirth et al. 2004
bushA	0.15	0.13	1.1	0.0	⋯	$1.15^{+0.19}_{-0.38}$	$7.60^{+0.20}_{-0.19}$	⋯

[a] Photometric redshift and 68% confidence region.
[b] $\log_{10}$ of the total stellar mass of the galaxy and 68% confidence region, with redshift fixed to the spec-z when available.
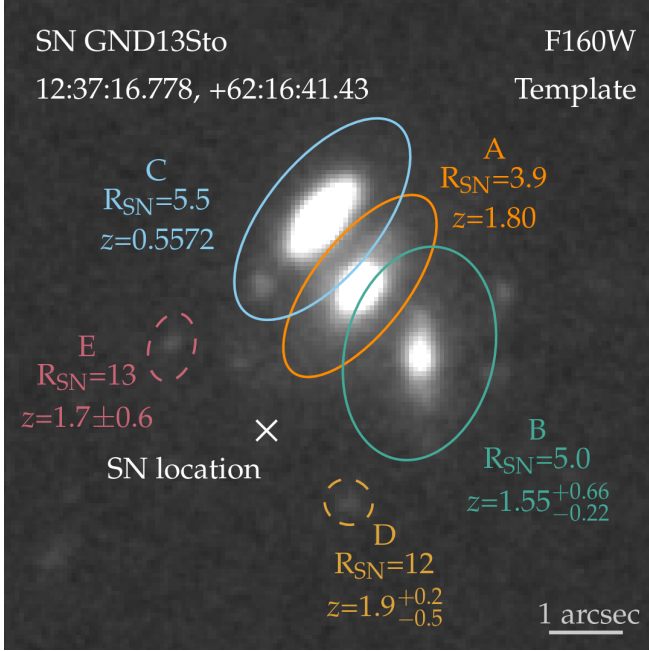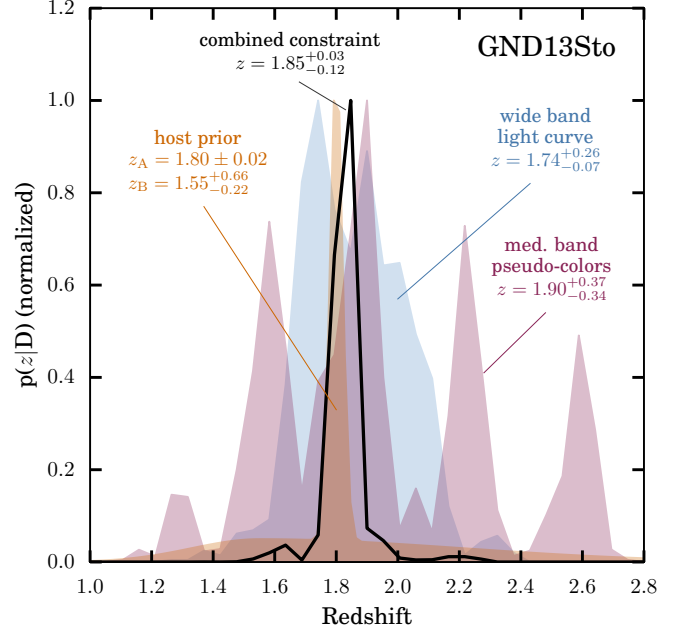
Figure 5. The host environment of SN GND13Sto. The template F160W image shown is a combination of all exposures from before MJD=56400 or after MJD=56600. Ellipses are drawn at $R = 2.5$ for the five nearest host galaxy candidates, using parameters measured with SExtractor in the F160W band (see Equation 1). Each host galaxy candidate is labeled with the R value of an ellipse that passes through the position of the SN, and the best available redshift constraint. As detailed in the text, galaxy A is the most probable host, while galaxies B, D and E all have broad photo-z distributions consistent with the redshift of galaxy A. Some or all of these four galaxies may be members of a small group hosting SN GND13Sto.


Figure 6. Redshift constraints on GND13Sto, assuming it is a Type Ia SN. The independent constraint from each of 3 different sources and the combined constraint are shown as probability distribution functions over redshift, all normalized to a peak value of 1.0. The composite redshift prior from host galaxy candidates A and B is given as a filled orange curve. The filled blue curve shows the marginal posterior probability from light curve fitting with only the wide-band data and no host galaxy redshift prior. The filled red curve shows the constraint from the single epoch of medium band data, along with the corresponding wide-band observations in the same epoch, but no host galaxy redshift prior. Finally, the solid black curve shows the composite redshift constraint derived from light curve fitting with all of the above information.

2013 in the GOODS-N field. There are 22 galaxies detected in the CANDELS F160W imaging that lie within $10''$ of the SN position, but none of these are coincident with the SN.

Using the R parameter (Equation 1) as an indication of the likelihood of physical association, we reduce the list of possible hosts to the 3 galaxies highlighted in Figure 5, which contain the SN position within an ellipse having $R < 10$. Of these, candidate A is the most likely, with $R = 3.9$, though host candidates B and C are close behind, with $R = 5.0$ and 5.5, respectively. Murphy et al. (2009) measured the redshift of galaxy A as $z = 1.82 \pm 0.02$, based on the IR spectrum from the InfraRed Spectrograph (IRS) on the *Spitzer* space telescope, and it was subsequently updated to $z = 1.80 \pm 0.02$ in Kirkpatrick et al. (2012). This IRS spectrum was also revisited by Hernán Caballero (2012), who used a maximum-likelihood spectral template fitting approach that confirmed the solution around $z = 1.8$. However, Hernán Caballero erroneously associated the IRS spectrum with SDSS J123716.59+621643.9 (our galaxy C) and thus incorrectly identified it as an outlier.

Host candidate B is separated from the SN by $R_{SN} = 5.0$, and has a photometric redshift of $z = 1.55^{+0.66}_{-0.22}$. Though quite broad, this photo-z overlaps the spectroscopic redshift of galaxy A, $z = 1.8$. There are two other galaxies within $10''$ of the SN (D and E in Figure 5) that also have very broad photometric redshifts consistent with galaxy A: $z = 1.9^{+0.2}_{-0.5}$ for galaxy D and $z = 1.7 \pm 0.6$

for E. These two low surface brightness galaxies are very unlikely to be directly associated with GND13Sto, as they are separated from the SN by $R_{SN} > 10$. Nevertheless, the similarity of these photo-z estimates suggests that galaxies A and B may be two dominant members of a small galaxy group containing D and E. Given the weak redshift constraints, this is very speculative, but if true then it is possible that SN GND13Sto is either bound to an undetected member of that group, or belongs to the intracluster light.

The only remaining galaxy near enough to be related to the SN is host candidate C. This is the galaxy SDSS J123716.59+621643.9, which has a spectroscopic redshift of $z = 0.5572$ from an optical spectrum (Wirth et al. 2004). We identify galaxy C as a foreground object because the SN photometry is inconsistent with this redshift: no normal SN light curve template at $z = 0.56$ can match the observed photometry with a χ^2 per degree of freedom (χ^2_ν) better than 3.3.

In summary, we find that GND13Sto is most likely associated with either galaxy A or galaxy B. If the former, then the SN is at redshift $z = 1.8$, and if the latter then the redshift is weakly constrained by the photo-z to $z = 1.55^{+0.66}_{-0.22}$. After classifying the SN in Section 4.2 we will revisit this redshift constraint in Section 4.2, bringing to bear all available information from the SN light curve, and also considering the possibility of an unseen host galaxy.
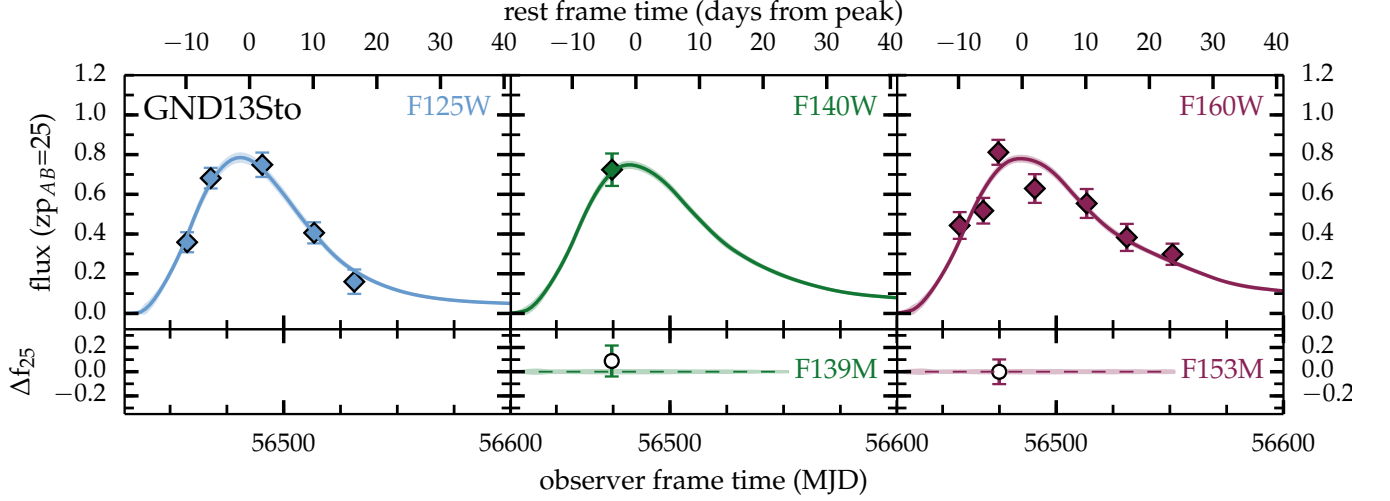
Figure 7. Infrared light curve of GND13Sto, showing flux as a function of time. Top panels show observations in HST wide-bands, in flux units normalized to an AB magnitude zero point of 25. Lower panels show *residual* fluxes for the corresponding HST medium-bands, after subtracting off the predicted flux from the best-fit model. The top axis marks rest-frame time at redshift $z = 1.8$. relative to the time of B band peak brightness.
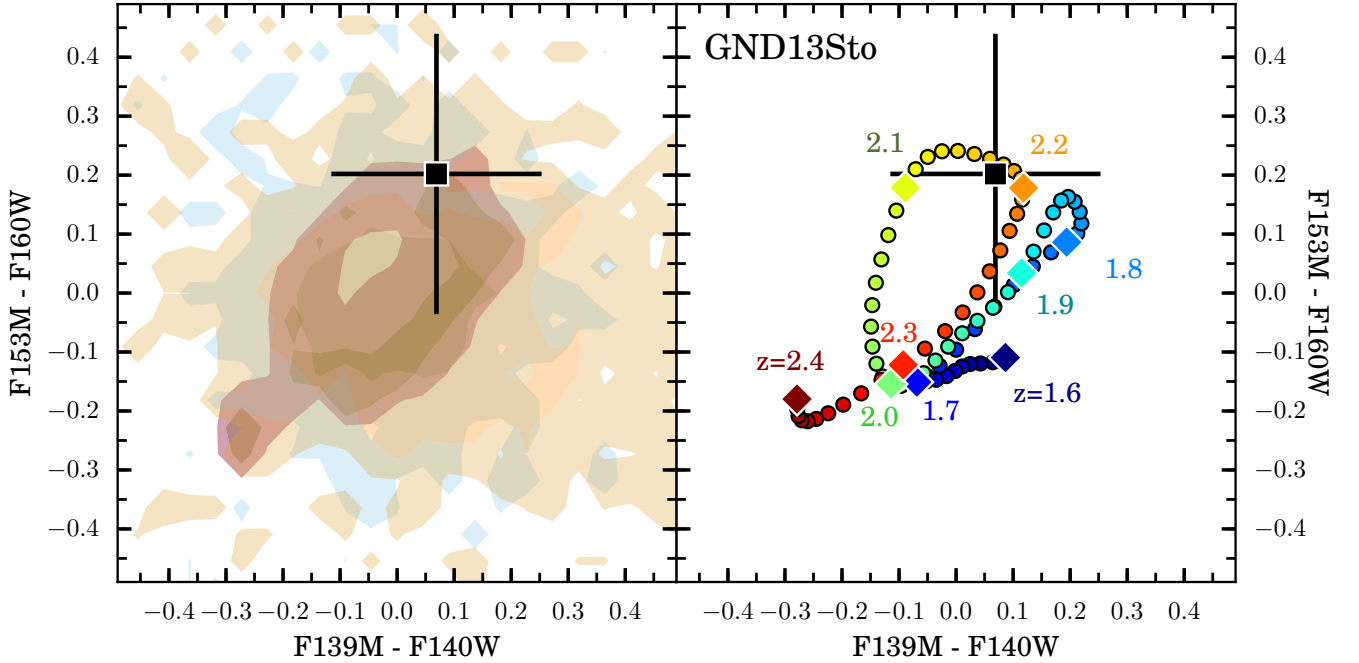
Figure 8. Medium-band pseudo-color circle diagrams for GND13Sto, as in Figures 2 and 3. In both panels, the observed colors for GND13Sto are indicated by the black square with error bars. (*Left*) Classification circle diagram: contours enclose 68% and 95% of the population for each class, with red for Type Ia, green for Type II and gold for Type Ib/c. The simulated SNe have redshifts that evenly sample the redshift range [1.6,2.4]. (*Right*) Redshift circle diagram : the line of colored points traces the pseudo-colors of a Type Ia SN from z=1.6 (blue) to z=2.4 (red), with diamond symbols marking each increment of 0.1 in redshift.

4.2. *GND13Sto Classification*

In the left panel of Figure 8 we consider the classification information provided by the medium-band circle diagram (developed in Section 2 and Figure 3). The observed medium-band pseudo-colors of SN GND13Sto are modestly offset from the origin in this pseudo-color space, locating it in the circular region where a Type Ia SN is expected to lie. The uncertainties are large, so although Figure 8 is suggestive of a Type Ia classification, by itself this evidence from medium-band pseudo-colors is far from definitive. Recall, however, that this information from the medium-band imaging is particularly valuable because it is insensitive to reddening and it is indicative of the presence or absence of specific absorption features in the SN's SED.

For a more complete classification picture, we next classify GND13Sto using a Bayesian photometric classification algorithm, as in R14. This classifier uses the `sncosmo` software package[20] to generate simulated SN light curves from spectrophotometric templates. We rely on the SALT2 model (Guy et al. 2010) to represent normal Type Ia SN, and use 42 spectrophotometric templates from the `SNANA` template library[21] (Kessler et al. 2009b) to represent CC SNe (26 Type II and 16 Type Ib/c). Although this template library is at present the best available collection of spectrophotometric models for CC SNe, it is an incomplete sampling of this heterogeneous population. It is possible to incorporate some knowledge about this incompleteness into the photometric classification framework (e.g. Rodney & Tonry 2009), but for this work we make the simplifying assumption that the library provides a nearly complete and evenly distributed sampling of CC SN properties.

For redshifts $z > 1.5$, the available templates (particularly those for CC SNe) do not extend far enough into the rest-frame UV to allow for a comparison to observations in ACS-WFC or WFC3-UVIS filters without extrapolating the templates. Thus, in this analysis we restrict our photometric classifications and light curve fitting to the available WFC3-IR observations, which correspond to rest-frame optical bands. As noted above, we have only upper limits for ACS and UVIS fluxes for both of these SN, so this stricture does not substantially diminish the available information.

We have made one important change in the classification algorithm relative to previous work, which is to eschew a luminosity prior. To get photometric classifications of the complete CANDELS/CLASH sample in R14 and Graur et al. (2014) we included a soft prior on the peak absolute magnitude as a function of redshift for each SN sub-class. The prior was based on the observed luminosity functions of these SN types in the local universe combined with an assumed cosmological model. This was necessary for the calculation of volumetric SN rates, as a large fraction of the sample has very limited photometric data (in some cases just 1-2 epochs with 2 or 3 bandpasses). Although in principle one could employ a weak prior without introducing a significant bias, in this work we have enough data such that we can get

robust classifications without the luminosity/cosmology prior. This ensures that these SNe can be used for cosmology without any concern of a bias introduced at the classification stage.

In the case of GND13Sto, we first classify the object using both wide- and medium-band photometry but including no redshift prior, and find that it is strongly classified as a Type Ia SN. The net classification probability for all CC SN sub-types is $< 1\%$, and no CC template can match the photometric observations with χ^2_ν better than 2.8. This agrees with our prior analysis in R14, where we found that GND13Sto is robustly classified as a Type Ia SN based on a Bayesian photometric classification using the wide-band light curves.

Our photometric classification apparatus can also accommodate a prior that infers the SN class based on the color and morphology of the host galaxy (Foley et al. 2013). In this case, using either of the plausible host candidates, galaxies A and B, we still find that GND13Sto is classified as a Type Ia SN with $> 98\%$ confidence.

4.3. *GND13Sto Redshift*

Due to the ambiguity of the host association, it is particularly valuable to evaluate the redshift constraints on GND13Sto independent of any host. As a first step, in the right panel of Figure 8 we consider the redshift information provided by the medium-band pseudo-color circle diagram (see Figure 2). Working now under the assumption that SN GND13Sto is a Type Ia SN, the location in the upper right corner of this pseudo-color space is most consistent with a redshift near $z = 1.85$ or near $z = 2.2$. Redshifts close to 1.7, 2.0, and 2.4 are disfavored by these data. Due to the low S/N of the medium-band observations for this SN, this diagram by itself is not definitive for redshift determination. However, as we will see, the addition of medium band observations to a complete wide-band light curve does provide a valuable improvement in the redshift precision, and supports an association with host galaxy A at $z = 1.8$.

In Figure 6 we build up a composite redshift constraint piece by piece, showing how the posterior probability distribution over redshift is separately restricted by the host galaxy, the wide-band light curve, and the colors from a single epoch that includes medium-band observations. First, the wide band light curve alone provides a fairly weak constraint, $z = 1.74^{+0.26}_{-0.07}$. Second, from the single epoch of medium-band pseudo-colors collected near peak brightness we derive a posterior probability distribution that is periodic in redshift. With only a single epoch, the *shape* of the light curve is unconstrained (i.e. any change in the value of x_1 could be reproduced by coordinated changes in x_0 and t_{pk}). To address this, we limit the range of t_{pk} to ± 3 days around the value inferred from the wide-band light curve fit – effectively adding in additional information by fixing the phase of the light curve at the time of the medium-band observations. Formally, we derive the redshift and uncertainty as $z = 1.90^{+0.37}_{-0.34}$, but Figure 6 shows that we actually have 4 peaks, at $z \sim 1.5$, 1.9, 2.2, and 2.6. This periodicity arises from spectral features moving in and out of the medium bands as the SN Ia template redshift changes, illustrated in Figure 2 and previously observed in S09. By combining the wide band light curve and the medium band epoch to-

---

gether, this redshift degeneracy is broken.

The final piece of redshift information we would like to include is a host galaxy redshift prior. Given that the host galaxy association is ambiguous, we use a composite redshift constraint that is the sum of the redshift probability distributions from host galaxy candidates A and B. In effect this allows an equal probability that the SN belongs to either galaxy, resulting in a sharp peak at z=1.8 (from host candidate A) and broad tails on either side (from host candidate B), as shown in Figure 6. Including this as a redshift prior, and utilizing all available SN photometry, we get a final redshift constraint of $z_{A+B} = 1.85^{+0.03}_{-0.12}$. To test how sensitive this redshift is to the host galaxy prior, we have also computed the redshift of GND13Sto using only the photometric redshift of host candidate B ($1.55^{+0.66}_{-0.22}$). This results in a posterior probability distribution that is peaked very close to the spectroscopic redshift of host candidate A: $z_B = 1.85^{+0.10}_{-0.19}$.

A final possibility to entertain is that the true host galaxy of SN GND13Sto is not detected in the CANDELS imaging data. Sullivan et al. (2006) found that 7% of the SNe in the SNLS program did not have a detected galaxy within $R_{SN} = 5$. Setting aside SN GND13Sto the equivalent "hostless" fraction is only 3% in the CANDELS/CLASH programs (Graur et al. 2014; Rodney et al. 2014), owing largely to the advantage of very deep HST imaging in these survey fields. Nevertheless, to consider the possibility of an unseen host, we repeat the redshift test using a flat prior, and find $z_{nohost} = 1.95^{+0.05}_{-0.26}$. Thus, even if the GND13Sto host is undetected, the SN photometry alone requires the redshift to be fairly close to the spectroscopic redshift of host candidate A (1.80±0.02).

We therefore conclude that the most likely scenario has SN GND13Sto as a Type Ia SN at $z = 1.80 \pm 0.02$. It may be bound to galaxy A, or associated with some possibly unseen component of a group containing that galaxy. At redshift $z = 1.80$ the best-fit SALT2 light curve parameters and uncertainties are $t_{pk} = 56482.0 \pm 1.2$, $x_1 = -0.48 \pm 0.70$, $c = 0.00 \pm 0.07$, and $m_B = 26.15 \pm 0.07$. Figure 7 shows this maximum likelihood Type Ia model, which has $\chi^2 = 11.4$ for 12 degrees of freedom.

4.4. *GND13Sto Lensing*

The foreground galaxy C at $z = 0.5572$ is separated from the SN by $2\farcs9$, making it a possible source of gravitational lensing for SN GND13Sto. Our procedure for estimating the lensing magnification follows Jones et al. (2013).

To define the lensing potential, we start with the stellar mass of the galaxy derived from SED fitting (Table 4) and use the broken power law relation of Yang et al. (2012) to convert this to the total mass of the dark matter halo. We then model the stellar component of the galaxy with a Sersic profile (Sérsic 1963) with parameters derived using GALFIT (Peng et al. 2002). Next, we assume an NFW density profile (Navarro et al. 1997) for the lensing potential, and use GRAVLENS (Keeton 2001) to generate 10,000 Monte Carlo realizations in which we vary the stellar mass of the lensing galaxy using the limits from SED fitting as reported in Table 4, and the

redshift of SN GND13Sto from section 4.3. Our Monte Carlo simulation also varies the mass-concentration relation and the stellar-to-halo mass ratio within their observed ranges (Guo et al. 2011; Yang et al. 2012). From this we infer a median magnification and 68% confidence limits of $1.02^{+0.02}_{-0.01}$ from the stoneC galaxy at the position of SN GND13Sto, indicating that the SN is not substantially biased by gravitational lensing. We include no correction for the insignificant magnification derived here, but see Section 7.2 for discussion of lensing effects on a full high-z SN sample.

5. GND12Col: SN COLFAX

5.1. *GND12Col Host Galaxy*

Our second high-z Type Ia SN candidate is GND12Col, [22] found in the CANDELS GOODS-N field on 27 May 2012. The nearest galaxy to the SN position, labeled host candidate A in Figure 9, has a relatively tight photo-z at $z = 2.35$, with 68.3% confidence interval [2.24,2.43].

Dahlen et al. (2013) recently demonstrated that even well-constrained photometric redshift estimates from any single SED fitting algorithm can be systematically biased and underestimate the redshift uncertainties, though a combination of photo-z estimates from multiple codes can reduce these concerns. To address this, we also fit the SED of the GND12Col host candidate A using the *BPZ* code, a Bayesian photometric redshift estimator (Benítez 2000). We derive a redshift probability distribution function, $P(z)$, centered at $z = 2.17$ with 68.3% confidence region [2.10,2.23], in good agreement with the photo-z derived above. We define the composite photo-z for host candidate A as a Gaussian centered at the mean of the two, with a 68.3% confidence region encompassing the mean of the two photo-z distributions: $z = 2.26 \pm 0.09$.

A second possible host galaxy – candidate B – is the large face-on spiral to the southeast, which has a spectroscopic redshift of $z = 0.9466 \pm 0.0002$ (Cowie et al. 2004). To determine whether galaxy A or B is the more likely host, we first evaluate the SN-galaxy separation independently of redshift using the R parameter of Equation 1. For host candidate A we find $R = 1.61$, and for host candidate B we have $R = 4.4$, supporting candidate A as the more likely host. Including the available redshift information strengthens this conclusion. GND12Col is $2.8''$ from the nucleus of host candidate B, which is 23 kpc at the redshift of that galaxy (assuming a flat ΛCDM cosmology with H_0=70, Ω_m=0.3). The SN is only $0.44''$ (3.3 kpc at $z \approx 2.2$) from the center of host candidate A. Based on this evidence, we assign host candidate A as the host of SN GND12Col, lending the SN a strong redshift prior at $z = 2.26 \pm 0.09$.

5.2. *GND12Col Classification and Redshift*

R14 classified GND12Col as a Type Ia SN, and we find that this classification holds up with improved photometry and is supported by the addition of medium-band observations. The formal Type Ia classification probability is effectively unity, with the combined probability for all common CC SN sub-classes limited to $< 10^{-6}$. Figure 10 shows the maximum likelihood Type Ia SN model

---

[22] Nicknamed "SN Colfax," after Schuyler Colfax, 17th Vice President of the United States.
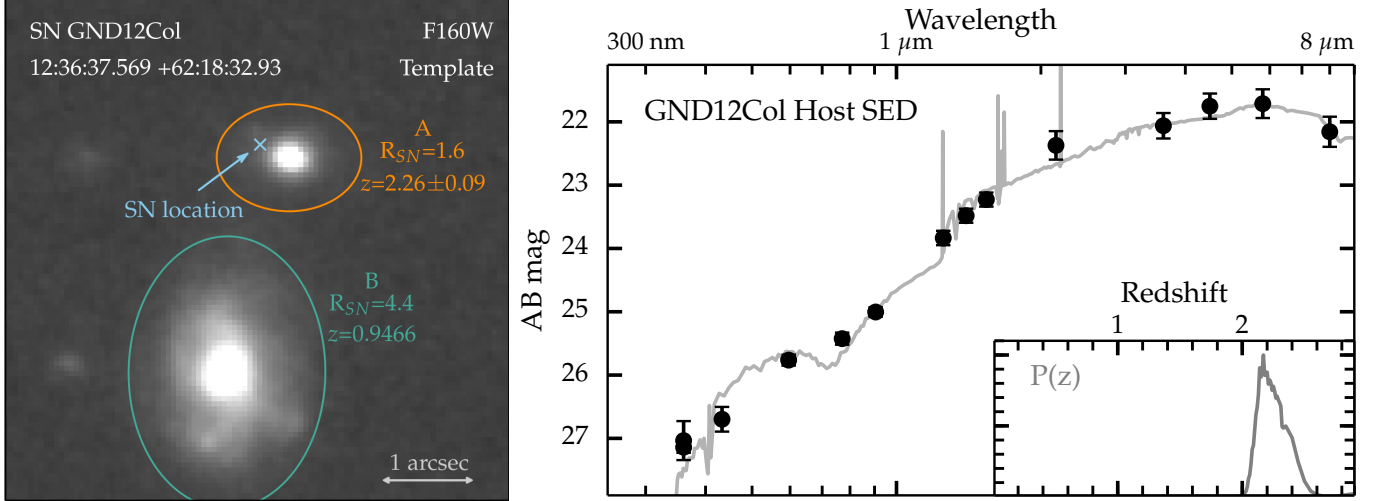
Figure 9. The host galaxy of GND12Col. *Left:* Template F160W image combining all exposures from before MJD=56000 or after MJD=56300. Ellipses are drawn at $R = 2.5$, using parameters measured using SExtractor in the F160W band (see Equation 1). Galaxy B is a foreground object. *Right:* Points show the observed photometry of the host, galaxy A, and the curve shows the best-fitting SED model. The inset at lower right shows the redshift probability distribution function derived using the LePhare SED fitting code, centered at $z = 2.26$, with a 68% confidence range of [2.17,2.35].
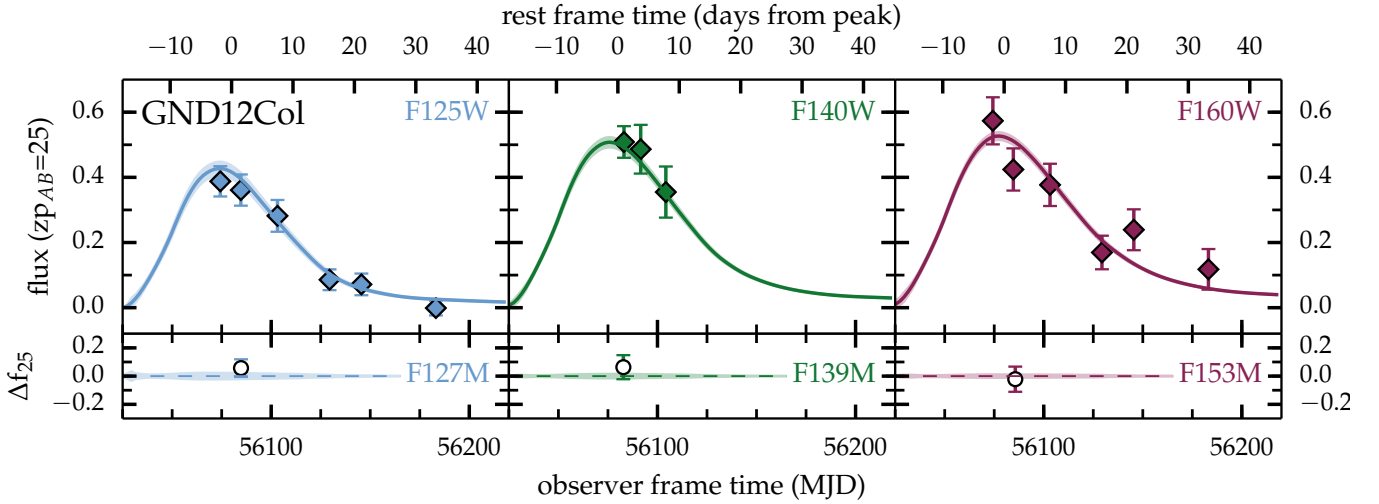
Figure 10. Infrared light curve of GND12Col, showing flux as a function of time. As in Figure 7 fluxes are normalized to zero point 25 and lower panels show residual fluxes for medium-band observations. The top axis marks rest-frame time at redshift $z = 2.26$.

at $z = 2.26$, which has χ^2=19.8 for 21 degrees of freedom. The best-fit SALT2 light curve parameters and uncertainties are $t_{pk} = 56078.6 \pm 5.4$, $x_1 = -0.13 \pm 1.14$, color $c = 0.08 \pm 0.12$, and peak apparent magnitude $m_B = 26.80 \pm 0.07$.

To visualize how the medium-band observations lead to an improvement of the GND12Col classification and redshift, we show in Figure 11 the position of the SN in a pair of 2D projections of the pseudo-color space. The CC SN population is expected to be spread out across the entire pseudo-color space, but in both of these slices we find GND12Col is conspicuously close to the narrower region occupied by Type Ia SNe. Note also that the SN position in both projections of pseudo-color-color space is consistent with the middle of the redshift distribution, i.e. $z \sim 2.2$.

Figure 12 shows how the posterior probability distribu-

tion over redshift for GND12Col is separately constrained by the host galaxy prior, the wide-band light curve, and the colors from a single epoch that includes medium-band observations. Each of these components alone provides a weak constraint, but all three are consistent and with the combination we achieve a precision of $\sigma_z = ^{+0.02}_{-0.10}$, on par with the best available photometric redshifts from well-sampled galaxy SEDs at similar redshift (Dahlen et al. 2013).

5.3. *GND12Col Lensing*

As in Section 4.4 we evaluate the possibility of gravitational lensing from the foreground galaxy B. This galaxy has a projected separation of $2''.8$, and a total stellar mass of $\sim 10^{10}$ M$_\odot$. As with GND13Sto, we adopt a Sersic profile for the stellar component and assume an NFW dark matter halo, with mass concentrations and stellar-
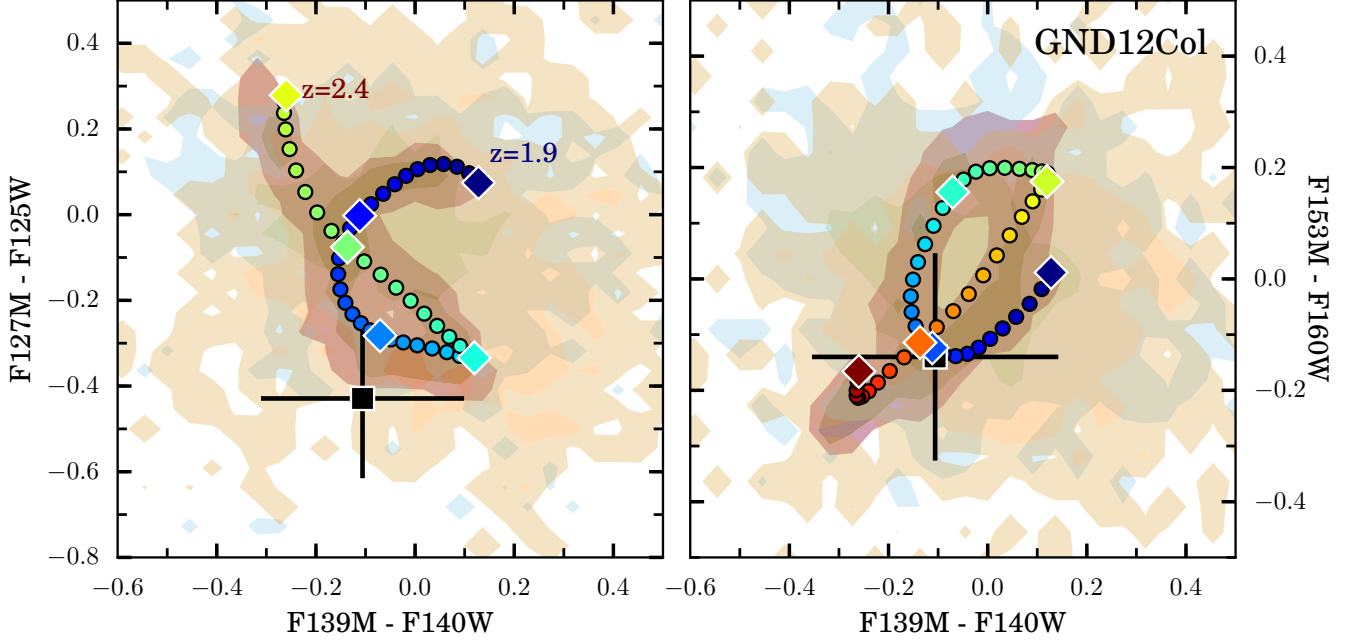
Figure 11. Medium-band pseudo-color diagrams for GND12Col, as in Figures 2 and 3. Contours enclose 68% and 95% of the population for each class, with red for Type Ia, green for Type II and gold for Type Ib/c. The simulated SN have redshifts that evenly sample the redshift range [1.9,2.4]. The line of colored points traces the pseudo-color of a Type Ia SN from z=1.9 (blue) to z=2.4 (red), with diamond symbols marking each increment of 0.1 in redshift. Observed colors for GND12Col are indicated by the black square with error bars.
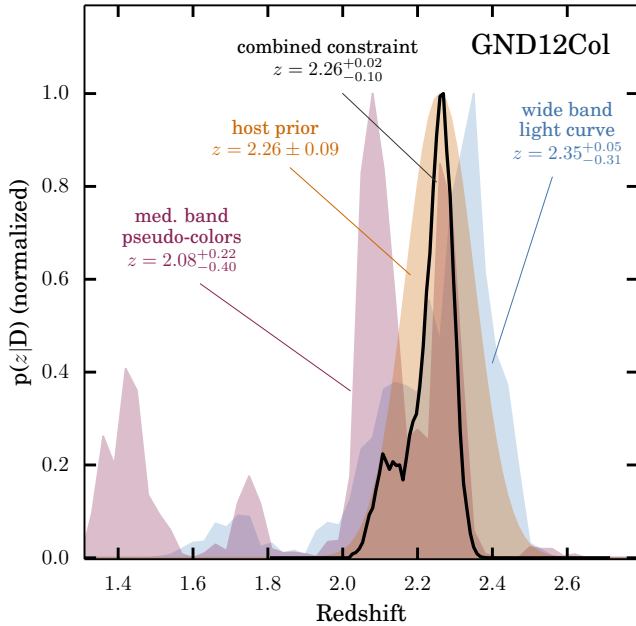
Figure 12. Redshift constraints on GND12Col. As in Figure 6, the filled orange curve shows the host galaxy redshift prior (from galaxy colfaxA), filled curves in blue and red show the constraints from the wide-band light curve and the medium-band colors (without including a redshift prior), and the solid black curve shows the composite constraint from all available data. All PDFs are normalized to a peak value of 1.0.

to-halo mass ratios following Guo et al. (2011) and Yang et al. (2012). From 10,000 Monte Carlo realizations of the lensing potential we determine a magnification factor

of $\mu = 1.04^{+0.03}_{-0.02}$. Once again we do not include a correction to the SN magnification for this mild magnification, but examine global lensing effects in Section 7.2.

6. EVALUATING THE MEDIUM-BAND PSEUDO-SPECTROSCOPY TECHNIQUE

For the two high-z Type Ia SNe discussed in this work, one may well ask whether the medium-band IR observations have provided significant value for the SN classification and redshift determination. After all, both of these objects were classified as Type Ia SN with high confidence in R14, and were assigned redshifts from their host galaxies, all without the benefit of the detailed medium-band analysis employed here.

Before scrutinizing the value of the medium band imaging in the following sections, let us first note that relative to photometric data the medium-band data are less susceptible to systematic biases. This is because (a) the medium-band pseudo-colors are insensitive to reddening (Figure 4) and (b) the redshift information in the medium-band data comes from individual spectral absorption features (Figure 2), not from the overall shape of the SED or the light curve.

6.1. Classification

A key practical benefit of the medium-band approach is that it can be used for efficient direction of scarce follow-up resources toward high-value targets. When a high-z Type Ia SN candidate is initially discovered, a single epoch of medium-band imaging can substantially clarify the classification picture while the SN is still close to peak brightness – as long as the redshift and time of peak are fairly well constrained. Thus, one can get a strong classification assessment for a relatively low cost

and then evaluate whether the candidate warrants an investment of additional follow-up time to collect the full wide-band light curves. Importantly, the medium band pseudo-colors are insensitive to dust (cf. Figure 4) and unaffected by the underlying cosmology. Thus, medium-band observations are similar to spectroscopy in that they can be used to select a Type Ia sample for follow-up without needing to invoke any priors on luminosity or color, which may carry a bias with redshift. The medium band classifications are therefore more robust than purely broad-band photometric methods, but more efficient than spectroscopy.

In addition to improving the SN redshifts, the medium-band data also add value by strengthening our photometric SN classifications. To see how large this effect is, we have done a piecemeal classification test: running subsets of each SN light curve through our Bayesian photometric classification algorithm both with and without the medium-band imaging data. Figure 13 shows the results. The value of the medium-band data in strengthening the classification is apparent in the first two columns of this figure. For these two tests we used just a single wide-band light curve (F125W or F160W) plus a single epoch of medium-band imaging (including the necessary observations in each complementary wide band). The addition of medium-band imaging alters the probabilities from a misleading or ambiguous $P(Ia|\mathbf{D}) \lesssim 0.5$ into a much more robust $P(Ia|\mathbf{D}) > 0.75$. In these cases the single-band light curve primarily constrains the time of maximum light, while the single-epoch medium-band pseudo-colors provides the majority of the classification information. In the third column of Figure 13, where the full multi-band IR light curve is available, the medium-band pseudo-colors do not alter the formal classification probability. This shows that the Type Ia classification can be securely established without any medium-band data, but to do so requires shape and color information afforded by multiple wide-band light curves extending over several months.

6.2. Redshift Determination

In Sections 4.3 and 5.2 we saw that the medium-band imaging improves the *accuracy* of the final redshift determination, by providing redshift constraints that are independent of the presumed host galaxy. In the case of SN GND13Sto, where the SN is widely separated from all nearby galaxies, the additional redshift constraint from medium-band pseudo-colors is especially valuable as a check against mis-identification of the host galaxy. For SN GND12Col – where we have no spectroscopic data on the host galaxy – the redshift information derived from medium-band imaging is very valuable to guard against a catastrophic error in the host galaxy photo-z, or misassociation with a galaxy that is actually in the foreground or background.

Figures 6 and 12 also demonstrate the value of medium band imaging to improve the *precision* of redshift constraints. For both GND13Sto and GND12Col the medium-band pseudo-colors deliver posterior redshift distributions with multiple peaks. As the broad single peak from the wide-band light curve breaks the degeneracy by picking out a single peak, the combination of wide- and medium-band imaging can reduce the photometric redshift uncertainty by almost a factor of 2. Redshifts
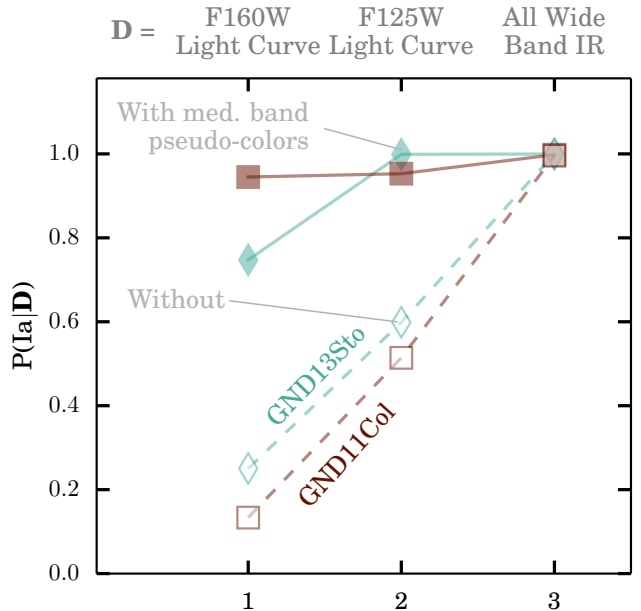
Figure 13. Examining the role of medium-band data in modifying the Type Ia classification probability for SN GND13Sto (blue diamonds) and GND12Col (red squares). Along each column we plot the Type Ia classification probability derived from a subset of the light curve data. For column 1 we use just the F160W band light curve (with and without a single epoch of medium-band pseudo-colors). Column 2 uses just the F125W band light curve, and column 3 uses all available wide-band IR data. Filled symbols with solid lines mark the results when including medium-band imaging data, and open symbols with dashed lines show the probabilities inferred without any medium-band data. In all tests we include a redshift prior derived from the nearest host galaxy candidate, but we add no prior on the time of peak brightness.

measured from the host galaxy can improve the precision still further, but if either of these SNe had no apparent host galaxy, then the medium band imaging would have been critical to make the SN useful for cosmology.

6.3. Future Surveys

For SN GND13Sto we collected exposures totaling $\sim$5 ksec (2 HST orbits) for each of 2 medium band filters (F139M and F153M). For GND12Col we used roughly 8 ksec (3 HST orbits) on each of 3 medium-band filters. In both cases we achieved a final S/N ratio between 5 and 10 in each individual filter, and we have seen that this is insufficient to provide a definitive classification by itself (e.g. Figures 8 and 11). To evaluate medium-band imaging for future surveys, it is instructive to consider how much exposure time would have been required to make the medium-band imaging pseudo-colors stand alone and deliver a robust classification without reference to the wide-band light curve at all.

To that end, we performed a Monte Carlo classification test in which we simulated medium-band observations for 2500 synthetic SNe spread evenly across the primary SN sub-classes, with redshifts between 1.6 and 2.4. Each simulated SN was "observed" through 3 medium bands and their complementary wide-band filters, with all observations taken concurrently in a single epoch within ± 15 observer-frame days of peak brightness. We then derive a Bayesian classification probability $P(Ia|\mathbf{D})$, tak-
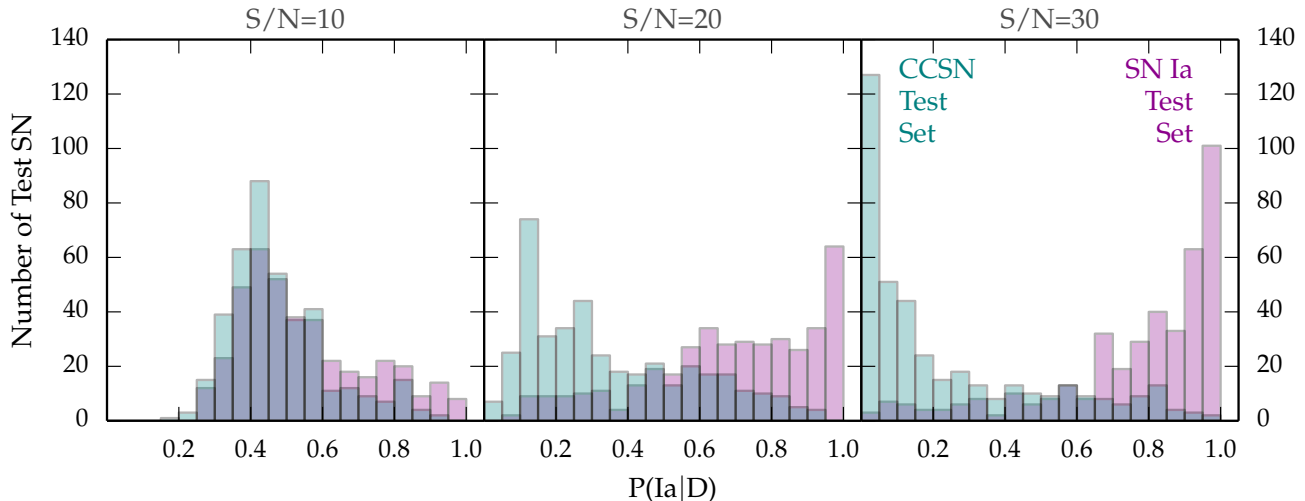
Figure 14. Results of a Monte Carlo simulation test examining the use of medium-band pseudo-colors alone for SN classification. Histograms show the distribution of Type Ia classification probabilities derived by classifying 2500 synthetic SN "test particles" using *only* a medium-band pseudo-colors. All SNe are simulated at redshifts in the range [1.6,2.4]. A single epoch of simulated observations are made in three medium band filters (F127M, F139M, F153M) and their corresponding wide-band counterparts (F125W, F140W, F160W), taken at ±15 observer-frame days from peak brightness. The blue histograms show classification results for simulated CC SNe and the red histograms count probabilities for synthetic Type Ia SNe. The test particles were simulated in three rounds, with the flux uncertainty in every band fixed to a S/N ratio of 10, 20, or 30 – shown in three panels from left to right.

ing care to avoid self-identification, where a synthetic SN yields an artificially good match when compared with the template that was used to create it. For CC SN test particles, this means that we remove from the template library the single template used to generate the CC SN test particle. For Type Ia SN test particles, we exclude from our comparison the range of SALT2 light curve shape and color parameters that are similar to the values generated for the test object. Here, "similar" is arbitrarily defined as a circle in $(x1, c)$ phase space centered on the test particle's $(x1, c)$ values, with radius 0.05.

Figure 14 shows histograms of the inferred type Ia classification probabilities, derived from a series of three Monte Carlo simulations. In each simulation we fixed the S/N to be 10, 20 or 30 for every individual filter. The progression of three panels in Figure 14 demonstrates the result that is to be naturally expected: as S/N is increased, the prospect of classification from medium-band data alone becomes more tenable. With S/N=10 in each band, the two simulated populations are indistinguishable. At S/N=20 the majority of synthetic Type Ia SNe are recovered, with $P(Ia|\mathbf{D}) > 0.75$ – but there is still substantial contamination from CC SNe being incorrectly classified. A large Type Ia sample defined using medium-band observations at S/N=20 would have a purity of $\sim 80\%$. When all observations attain S/N=30, the populations are much more distinct, and it would be possible to define a Type Ia SN sample with $>95\%$ purity using such high-quality medium-band data.

Realistically, these S/N targets are not achievable with HST for targets like SN GND13Sto and GND12Col. To reach S/N=20 for a Type Ia SN at z=2.0 with an F160W AB mag of 26 would require a total of roughly 100 ksec (40 HST orbits) spread across three medium bands and their wide-band counterparts. For S/N=30, the exposure time requirement rises to ~ 215 ksec (nearly 90 HST orbits). At those costs, grism spectroscopy may become

an appealing alternative, especially since it delivers more ancillary science benefits in any given field. Given the limitations of finite observing time, the best strategy for HST medium-band imaging may be the one used in this work: relatively short observations that are not definitive in themselves, but provide support for a holistic approach to photometric classification and redshift determination.

The small set of medium-band IR filters on HST currently limits the application of the medium-band pseudo-spectroscopy method to SNe at $z \sim 2$. The JWST Near-infrared Camera (NIRCAM) will have 12 medium-band filters from 1.5 to 5 μm, substantially expanding the reach of this technique and the potential for testing models of time variable dark energy or Type Ia SN evolution. In principle, JWST medium band filters could be used to characterize Type Ia SN candidates as far as $z \sim 6$. Unfortunately, the diminishing cosmic star formation rate density at very high redshifts will make these objects few and far between, so the initial discovery will be more efficiently done with a wide-field observatory, such as Euclid or WFIRST-AFTA. With this combination of Euclid/WFIRST and JWST, it will be possible to discover and characterize a sample of *primordial* Type Ia SNe– explosions of the very first generation of binary white dwarfs – which in turn would enable the most stringent possible test for the secular evolution of Type Ia SN properties.

7. THE HIGH-Z FRONTIER FOR TYPE IA SN COSMOLOGY

The two objects presented here are among the most distant Type Ia SNe known, with GND12Col now setting the bar with the highest redshift. As such, these SNe are of great interest for testing cosmological models and evaluating possible systematic biases that may be suppressed or obscured at lower redshifts. In this section we begin with an extension of the Hubble diagram in Section 7.1, and then examine some of the particular

considerations that must be addressed when incorporating such high-z SNe into a cosmological sample.

7.1. *Extending the Hubble Diagram*

In Figure 15 we plot a Hubble residuals diagram, showing the luminosity distance relative to ΛCDM versus redshift. The baseline cosmology is defined by fitting to a collection of 943 Type Ia SNe from the literature (Riess et al. 1999; Jha et al. 2006; Hicken et al. 2009; Kessler et al. 2009a; Contreras et al. 2010; Folatelli et al. 2010; Conley et al. 2011; Stritzinger et al. 2011; Hicken et al. 2012; Ganeshalingam et al. 2013; Rest et al. 2014). We fit these light curves using the SALT2 model, and define a corrected apparent B-band peak magnitude following Tripp (1998): $m'_{\rm B} = m_{\rm B} + \alpha x_1 - \beta c$. Here the (uncorrected) peak apparent magnitude $m_{\rm B}$, the light curve width x_1, and the color c are derived from the light curve fit. For this exercise we fixed the SALT2 model parameters to the values derived in the Rest et al. (2014) analysis of the PS1 SN sample: $\alpha = 0.147$ and $\beta = 3.13$. We then subtract $m_{\Lambda CDM}$, the apparent magnitude predicted by a flat ΛCDM cosmology at each redshift, with the Type Ia SN peak absolute magnitude at a fiducial value of $M_B = -19.34$, and using best-fit values of $\Omega_{\rm m}$=0.284 and H_0=70.88. The SN magnitude errors shown in Figure 15 also include an intrinsic scatter of $\sigma_{\rm int} = 0.12$ magnitudes (Scolnic et al. 2014; Betoule et al. 2014), and for simplicity this term is not separately defined for each survey. These simplifications allow for an expedient comparison of the new high-z Type Ia SNe against existing SN and a baseline cosmological model. A more complete examination of cosmological models will be presented in a subsequent paper (Riess et al., in prep).

7.2. *Gravitational Lensing*

As Type Ia SN observations are pushed to higher redshifts, observed SN fluxes are increasingly affected by gravitational lensing. Photons in the Universe are conserved, so when sampling a sufficiently large number of random sight lines, the mean SN flux is unperturbed. Thus, lensing adds scatter to Type Ia SN distances, but if treated appropriately it does not bias cosmological inferences (Holz 1998).

Lensing can be handled in one of two ways: either (a) rely on a large sample to average out the bias, while accounting for the increased scatter, or (b) estimate the (de)magnification along every line of sight and include appropriate corrections. Holz & Linder (2005) examined the former option and found that lensing introduces an additional redshift-dependent dispersion in the observed Type Ia SN fluxes of $\sigma_{\rm lensing} = 0.088z$ (or $0.093z$ if treating intrinsic Type Ia SN dispersion as Gaussian in magnitude).

A formalism for individual lensing corrections (option b) was presented in Gunnarsson et al. (2006), in which galaxy detections from deep imaging surveys are used to model dark matter halos that intersect each SN sight line. Jönsson et al. (2006) applied this method to 33 SNe from the HST GOODS survey (Strolger et al. 2004; Riess et al. 2004b) and demonstrated that such lensing corrections can indeed reduce the lensing scatter. Additionally, Jönsson et al. found that the mean magnification factor in the HST sample was consistent with unity, implying that there is no evidence for a bias towards including highly magnified objects in the high-z SN cosmology sample.

In this work we have found no evidence for significant lensing from the nearest detected foreground galaxy to each SN (Sections 4.4 and 5.3). However, the nearest foreground galaxy is not the only possible source for gravitational lensing perturbations. For a more precise lensing correction, one should include all foreground sources out to $\sim 1'$(Gunnarsson et al. 2006; Jönsson et al. 2006).

As we are not pursuing a measurement of cosmological parameters in this work, we adopt option (a) from above, applying the $0.093z$ mag additional scatter from Holz & Linder (2005) as an additional noise term for all SN shown in Figure 15. For our two high-z Type Ia SNe this corresponds to 0.17 mag at the redshift of GND13Sto and 0.2 mag for GND12Col. It is noteworthy that in this high redshift regime we have transitioned to a point where the scatter from gravitational lensing along the line of sight is larger than the intrinsic scatter of the Type Ia SN population (~ 0.12 mag) – though for these individual objects both of those error terms are dwarfed by the observational uncertainties.

7.3. *Biases and Evolution*

At the high-z edge of any survey, a selection bias may be introduced as intrinsically faint objects are more likely to slip below the detection threshold and be missed (Malmquist 1920). The blue shaded regions in the upper right corner of Figure 15 show the redshift and luminosity regime where such a bias could begin to remove Type Ia SNe from our sample. These regions are defined by simulating a fiducial Type Ia SN ($x_1 = 0$, $c = 0$) at each redshift and measuring the *visibility time*, $t_{\rm vis}$: the number of observer-frame days where the SN is brighter than the 50% detection efficiency threshold of the CANDELS SN search (26.5 AB mag in F125W and F160w, see R14). In the light blue region, our fiducial Type Ia SN model has a visibility time shorter than the typical cadence of the CANDELS survey (50 days). In the dark blue region, the visibility time drops below zero, meaning that normal Type Ia SNe are effectively undetectable. This does not paint a complete picture of the Malmquist bias, as these regions depend on the light curve shape and color, but this illustration shows that the absence of positive Hubble residuals at $z > 1.5$ should be unsurprising, given the measured detection limits of this survey.

In a subsequent paper, we will present distances for the complete sample of high-z Type Ia SNe from CANDELS and CLASH, comprising $\sim$15 Type Ia SNe at $1 < z < 1.7$ (Riess et al. in prep). Further high-z Type Ia SNe will be delivered by ongoing HST surveys such as the *FrontierSN* program (PI:Rodney) and the *See Change* survey (PI:Perlmutter). These extensions of the Type Ia SN sample at $z \sim 1.5$ will improve the sensitivity of Type Ia SN cosmology, especially in testing for a time-variable dark energy equation of state (the ratio of pressure to density, $w = P/\rho$). Salzano et al. (2013) quantified how much these and future surveys can be expected to refine our constraints on w. Adopting a common parameterization that is linear with the scale factor, $w = w_0 + w_a(1-a)$ (Chevallier & Polarski 2001; Linder 2003), Salzano et al. found that a sample of ~ 30 Type Ia SNe at $z > 1$ should reduce the uncertainty on w_a by $\sim 20\%$.
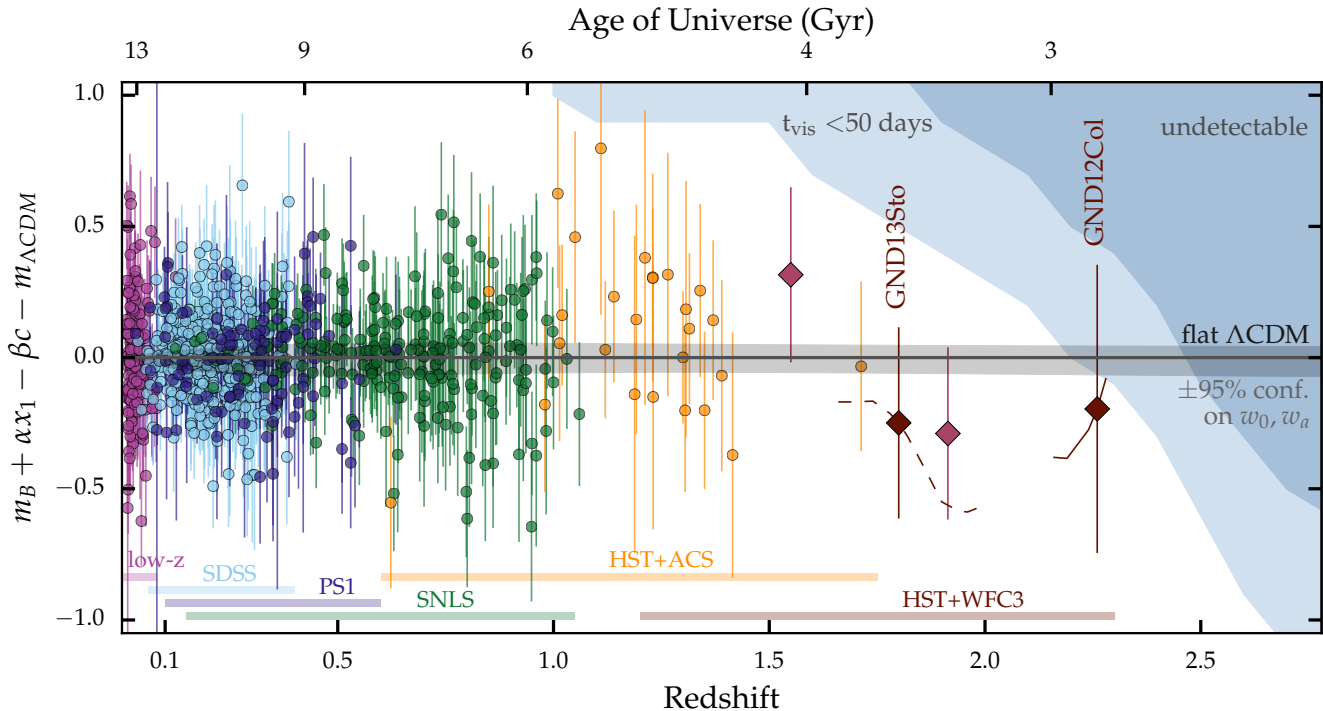
Figure 15. Hubble residuals diagram, plotting as a function of redshift the apparent magnitude (corrected for light curve shape and color) relative to the predicted magnitude from a flat ΛCDM cosmology. Colored circles show a compilation of $\sim$900 SNe from the low-redshift CfA and CSP surveys (Hicken et al. 2009; Stritzinger et al. 2011), SDSS (Kessler et al. 2009a), PS1 (Rest et al. 2014), SNLS (Conley et al. 2011), and at $z > 1$ the orange circles are from the GOODS and SCP surveys using the ACS camera on HST (Riess et al. 2007; Suzuki et al. 2012). Red diamonds at z=1.55 and 1.91 plot two previously published Type Ia SNe from the CANDELS survey (Rodney et al. 2012; Jones et al. 2013), and dark red diamonds at $z = 1.8$ and 2.26 show the two new Type Ia SNe from this work. All vertical error bars include a uniform intrinsic dispersion of $\sigma_{\rm int} = 0.12$ mag and a redshift-dependent gravitational lensing dispersion of $\sigma_{\rm GL} = 0.093z$. For SN GND13Sto and GND12Col the x-axis error bar is shown as a curved line to indicate the covariance of distance with redshift for this object (dashed for GND13Sto to indicate that this redshift range only applies if the association with host galaxy A is presumed to be spurious). The shaded region in the upper right demarcates the space where the CANDELS survey starts to lose sensitivity for discovery of Type Ia SNe (see text for details).

It is naturally expected that the *demographics* of the observed Type Ia SN population should change with redshift, as brighter Type Ia SNe with slower light curves are more prevalent in star-forming galaxies, which dominate the universe at $z > 1$ Howell et al. (2007). Such a shift in the composition of the Type Ia SN population should not by itself introduce any cosmological bias. However, it is also possible that differences in the progenitor systems for high z Type Ia SNe could lead to luminosity biases – deviations from the expected standard candle relations between shape, color and luminosity. Indeed, one of the original motivations for this high redshift SN observing program was to detect SNe in the early universe where such effects could be disentangled from cosmological changes (Riess & Livio 2006).

Using the full CANDELS and CLASH Type Ia SN sample, R14 found evidence that the fraction of Type Ia SNe exploding within 500 Myr after formation is $\lesssim$ 50%. This means that a substantial fraction of all the Type Ia SNe that we might observe at $z \sim 2$ could have been formed when the universe was < 2 Gyr old, perhaps in very low metallicity environments. The mean mass of a Type Ia SN progenitor star must also increase with redshift, as slow-evolving low-mass progenitors have less time available to leave the main sequence and start accreting mass as a white dwarf. It is conceivable that such changes in the progenitor mass or metallicity could lead to a sys-

tematic shift in the peak magnitudes that is not correlated with the light curve width or color (Domínguez et al. 2001; Timmes et al. 2003; Riess & Livio 2006). Finding evidence for this effect is more challenging than improving constraints on variable dark energy models. Salzano et al. (2013) found that testing plausible models for non-cosmological evolution of the Type Ia SN population requires $\sim$50 SNe at $1.5 < z < 3.5$, which could first be done with the *James Webb Space Telescope* (JWST), scheduled for launch in 2018.

8. SUMMARY

In this work we have presented two primary results, where the first is methodological and the second observational:

1. a description of the use of HST medium-band IR filters for analyzing high-z SNe; and

2. the discovery, classification, and redshift determination for two of the most distant Type Ia SNe yet known.

We have demonstrated that the medium-band technique can provide an alternative to costly spectroscopic observations of high-z SNe. This method capitalizes on the semi-periodic nature of the broad absorption features in Type Ia SN SEDs and provides a *photometric*

tool for examining *spectroscopic* features. For classifying and determining redshifts of high-z SNe, this technique is more efficient than spectroscopy but more precise than photometry. By relying on difference imaging, we avoid contamination from host galaxy light that can plague SN spectroscopy. By using medium-minus-wide pseudo-colors, this approach does not sample the broad-band SED colors and is therefore insensitive to dust extinction.

For the second component of this work, we have marshaled all available wide- and medium-band photometry and host galaxy information to determine that SN GND13Sto and GND12Col are both Type Ia SNe at $z \sim 2$. These objects push the frontier for Type Ia SN cosmology into an era when the Universe was only 3 Gyr old. Although the uncertainties are large, we find that both are fully consistent with a standard flat ΛCDM cosmology, showing no obvious deviations that might arise from extreme evolution of the Type Ia SN progenitor population. We leave a more robust examination of cosmological models to future work, which will incorporate the full CANDELS and CLASH SN samples (Riess et al. in prep).

Whereas the SN samples at $z < 1$ are moving quickly toward the "big data" era, the high-z regime is still very much limited by the sample size. With these high-z objects at the redshift frontier, each requires careful attention to accommodate the unique nuances of classification and redshift estimation. Infrared imaging surveys from HST, JWST and successor observatories should continue to expand the sample of such high-z SNe in coming years. A decade from now the high-z regime may well look like the $z < 1$ samples of today, with hundreds or thousands of well-sampled Type Ia SNe from observatories such as NASA's planned WFIRST-AFTA. That will open up the exciting possibility of exploring a wider range of cosmological models and evolution scenarios with these early-universe SNe.

APPENDIX

GSD11Bus

Detected in the CANDELS GOODS-S field, GSD11Bus[23] appeared in a very low surface brightness host galaxy (26.8 AB mag arcsec^{-2} in the F160W band). The host also has a red SED, with a V-H color of approximately 1 mag. Identification of the 4000 Å break across the *riz* bands leads to a central peak in the photo-z at $z = 1.15$ as shown in Figure 16. However, the large photometric uncertainties allow for other possible solutions at $z \sim 0.3$, 0.8 and 2.1. No spectroscopic constraint on the host redshift is available.

The SN was initially classified as a possible SN Ia at $z > 1$ based on its very red optical-IR colors. This prompted follow-up imaging with HST, using both medium and wide bands. However, with the full light curve this object was found to be inconsistent with being a normal SN Ia anywhere in the allowed redshift range. R14 classified GSD11Bus as a Type Ib/c, with a redshift of $z = 1.7 \pm 0.1$ based on the combination of the host photo-z and the SN light curve.[24] Using our improved photometry (Table 5), we revisit this classification, and find again that GSD11Bus is incompatible with SN Ia models. The classification probabilities are P(Ia|$\mathbf{D}$)=0.03, P(Ib/c|$\mathbf{D}$)=0.92, and P(II|$\mathbf{D}$)=0.05. The best-fit light curve model shown in Figure 17 is based on the Type Ic SN 2006fo from the SDSS SN survey (SDSS ID 13195, Zheng et al. 2008). At $z = 1.15$ this model provides a good fit to the optical+IR light curve, with $\chi^2_\nu = 0.85$.

Figure 18 shows the redshift constraints on GSD11Bus from the wide-band light curve, medium-band colors, the host photo-z, and the combined constraint from all sources. Without the host prior, the light curve constraints would favor a redshift at $z = 1.6$ or 0.8. These redshifts also require a CC SN classification, so although the host and light curve constraints are not in agreement, there is no plausible solution in which GSD11Bus can be classified as a Type

---

[23] Nicknamed "SN Bush" after the 41st and 43rd Presidents of the United States.
[24] In R14 the photo-z for the GSD11Bus host galaxy was re-

ported as $z = 1.76 \pm 0.53$, based on an earlier version of the SED.
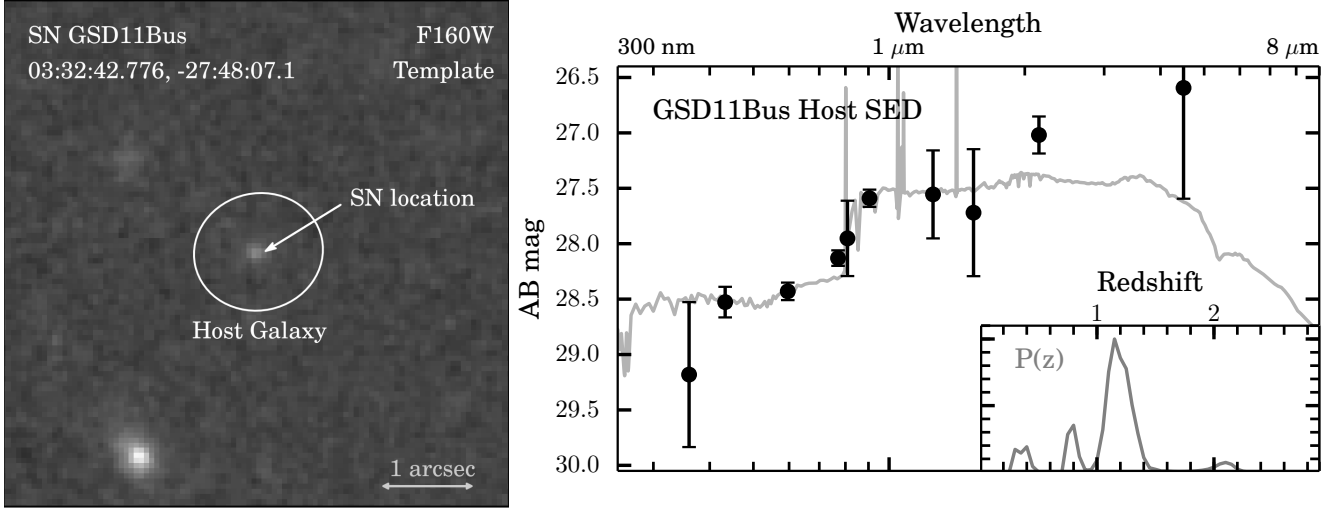
Figure 16. The host galaxy of GSD11Bus. *Left:* The F160W template image, constructed from all exposures before MJD=55720 and after 55600. The ellipse encloses ∼90% of the host galaxy flux in the F160W band. *Right:* Filled points show the observed SED of the GSD11Bus host galaxy and the gray curve is the best-fitting SED model. The inset shows the photometric redshift probability distribution, peaked at z=1.15.

Table 5
GSD11Bus Photometry

Obs. Date (MJD)	Filter	Exp. Time (sec)	Flux (counts/sec)	Flux Err (counts/sec)	AB Mag[a]	Mag Err	AB Zero Point	ΔZP[b] (Vega-AB)
55720.1	F606W	5211	0.0623	0.0497	29.506	0.865	26.493	-0.086
55723.0	F606W	5211	-0.2223	0.0546	>28.5	⋯	26.493	-0.086
55795.2	F606W	1007	0.0968	0.1053	>27.7	⋯	26.493	-0.086
55720.2	F814W	5808	-0.0921	0.0633	>27.8	⋯	25.947	-0.424
55770.9	F814W	1886	0.3049	0.0864	27.237	0.308	25.947	-0.424
55795.1	F814W	932	0.4176	0.1057	26.895	0.275	25.947	-0.424
55847.7	F814W	480	-0.4589	0.1879	>26.6	⋯	25.947	-0.424
55720.0	F850LP	2046	-0.0480	0.0566	>26.8	⋯	24.857	-0.519
55722.9	F850LP	2046	-0.2579	0.0694	>26.6	⋯	24.857	-0.519
55803.2	F098M	2512	0.4756	0.0766	26.474	0.175	25.667	-0.562
55803.9	F105W	1256	1.2029	0.1465	26.068	0.132	26.269	-0.645
55892.5	F105W	8395	0.2638	0.0774	27.716	0.319	26.269	-0.645
55718.1	F125W	1006	0.1360	0.1691	>27.0	⋯	26.230	-0.901
55778.8	F125W	1006	0.9312	0.1593	26.308	0.186	26.230	-0.901
55795.1	F125W	1006	1.0172	0.1556	26.212	0.166	26.230	-0.901
55803.1	F125W	1256	1.2903	0.1558	25.953	0.131	26.230	-0.901
55819.6	F125W	1006	0.9515	0.1565	26.284	0.179	26.230	-0.901
55854.2	F125W	1006	0.5491	0.1548	26.881	0.306	26.230	-0.901
55869.9	F125W	1006	0.3475	0.1442	27.378	0.451	26.230	-0.901
55923.2	F125W	1006	0.4099	0.1440	27.198	0.382	26.230	-0.901
55974.6	F125W	1006	0.2356	0.1477	27.800	0.681	26.230	-0.901
55803.3	F127M	2512	0.2966	0.0658	25.961	0.241	24.641	-0.961
55803.3	F139M	2512	0.3664	0.0725	25.569	0.215	24.479	-1.079
55803.9	F140W	1256	1.6063	0.2136	25.937	0.144	26.452	-1.076
55847.8	F140W	812	0.9162	0.2536	26.547	0.300	26.452	-1.076
55803.8	F153M	2512	0.3983	0.0776	25.463	0.211	24.463	-1.254
55718.1	F160W	1056	0.0097	0.1468	>26.8	⋯	25.946	-1.251
55778.8	F160W	1006	0.7075	0.1900	26.322	0.291	25.946	-1.251
55795.1	F160W	1006	1.0666	0.1808	25.876	0.184	25.946	-1.251
55803.1	F160W	1256	1.0519	0.1437	25.891	0.148	25.946	-1.251
55819.6	F160W	503	0.8344	0.2442	26.143	0.318	25.946	-1.251
55854.2	F160W	1156	0.9717	0.1809	25.977	0.202	25.946	-1.251
55869.9	F160W	1056	0.5799	0.1598	26.538	0.299	25.946	-1.251
55923.2	F160W	1006	0.0633	0.3185	>26.0	⋯	25.946	-1.251
55974.6	F160W	1206	0.1534	0.1777	>26.6	⋯	25.946	-1.251

[a] For flux values of less than 1σ significance we report the magnitude as a 3σ upper limit
[b] Zero point difference: the magnitude shift for conversion from AB to Vega magnitude units.
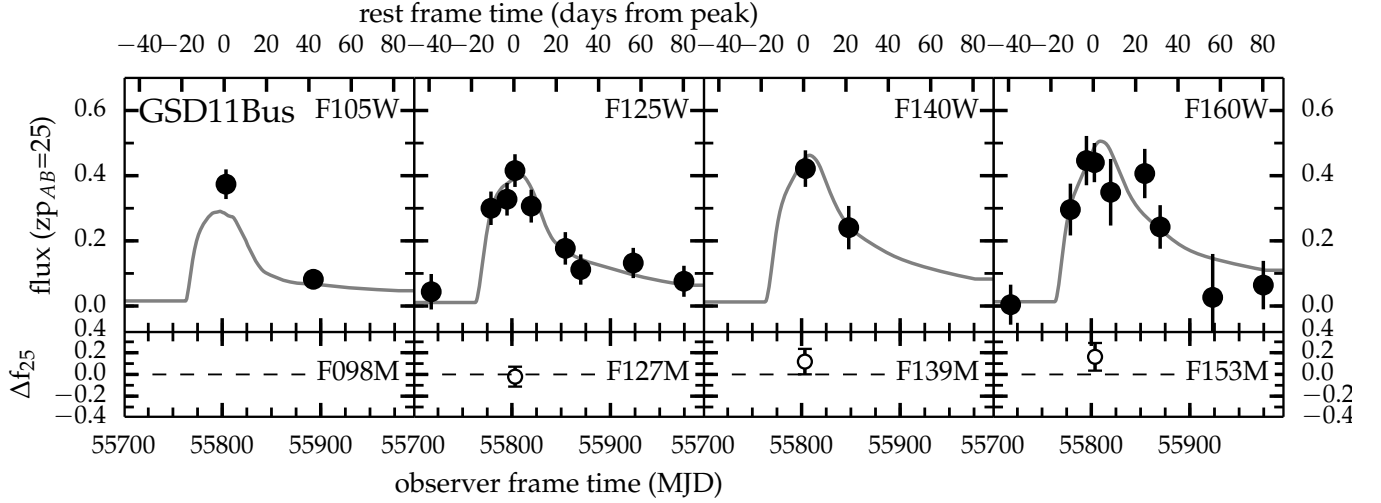
Figure 17. Infrared light curve of GSD11Bus, showing flux as a function of time. As in Figures 7 and 10 fluxes are normalized to zero point 25 and lower panels show residual fluxes for medium-band observations. The top axis marks rest-frame time at redshift $z = 1.15$. Grey curves show the best-fit model, based on the Type Ic SN 2006fo.
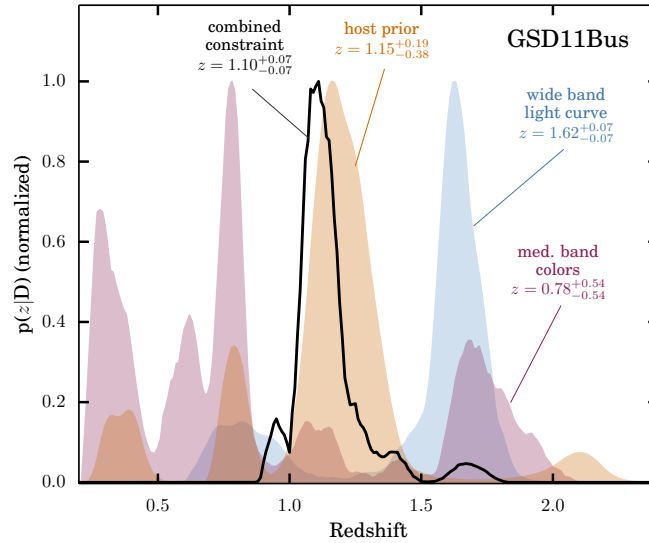

Figure 18. Redshift constraints on GSD11Bus. As in Figures 6 and 12, the independent constraint from each of 3 different sources and the combined constraint are shown as probability distribution functions over redshift, all normalized to a peak value of 1.0.

Ia. The Type Ia classification is strongly disfavored principally because the slow decline of the light curve favors a high redshift, which is incompatible with the observed fluxes in the ACS F814W and WFC3-IR F105W bands. This is reinforced by the medium-band colors, shown in Figure 19, which locate GSD11Bus in a region of pseudo-color space that is well removed from the Type Ia SN locus.

   Although this evidence is sufficient to rule out a Type Ia classification, one may be concerned that the GSD11Bus medium band pseudo-colors place it outside of the 95% contours for *all* SN classes, as shown in the left panel of Figure 19. It is possible that GSD11Bus is simply a statistical outlier, but we must caution that this discrepancy may be indicative of a fundamental problem with the library of CC SN templates employed in this work. Although the template library includes 26 Type II templates, these are all based on a set of just 3 spectral time series (Gilliland et al. 1999; Di Carlo et al. 2002; Baron et al. 2004). Each template was generated by warping those few spectral time series to match the well-sampled broad-band photometry of 26 low-z SN. In this way, the broad-band colors of our simulated SNe can be expected to accurately represent the diversity of broad-band colors from this population. However, the diversity of emission line strengths may not be well represented in this library, as the warping procedure is not sensitive to such features.

   Although we have classified GSD11Bus as a Type Ib/c object, the light curve may also be consistent with the Type II-L or IIn sub-classes, which are under-represented in our template library. For those cases, the strong Hα feature
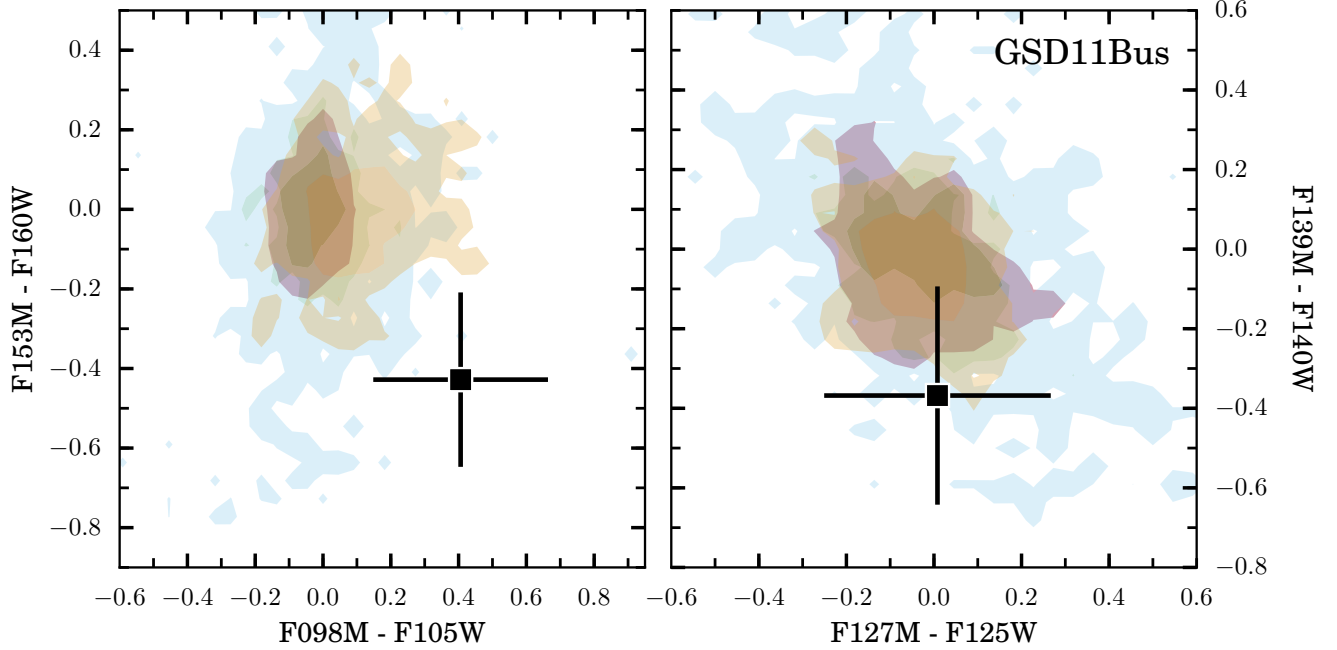
Figure 19. Medium-band color-color diagrams for SN GSD11Bus, as in Figure 3. Contours enclose 68% and 95% of the population for each class, with red for Type Ia, green for Type II and gold for Type Ib/c. The simulated SN have redshifts that evenly sample the redshift range [0.7,1.5], encompassing the two primary peaks of the host galaxy photo-z. Observed colors for GSD11Bus are indicated by the black diamond with error bars.
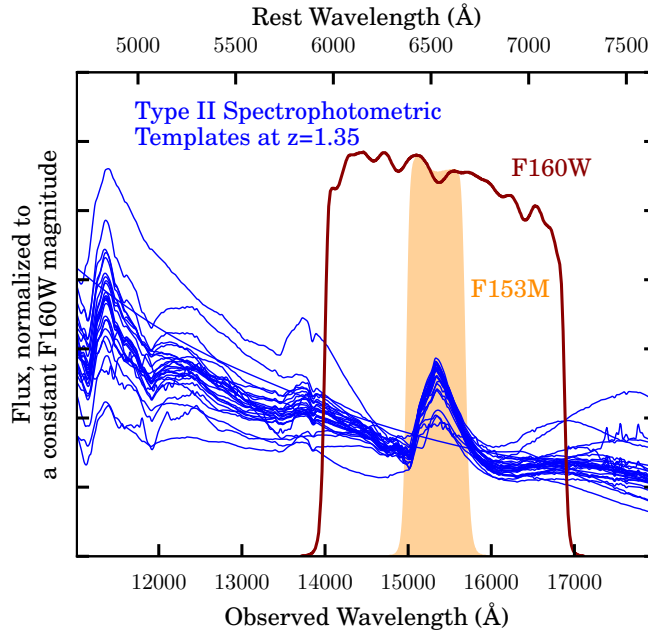
Figure 20. Demonstrating the lack of spectral diversity in the Type II template library employed in this work. All Type II spectrophotometric templates are shown as blue lines, redshifted to $z = 1.35$ and observed at +6 days after peak brightness (a redshift and age consistent with the SN GSD11Bus data). Each template spectrum is normalized to have the same integrated flux through the F160W bandpass, which is shown as a solid red line. At this redshift the Hα line occupies the entire F153M bandpass, which is shown as the orange shaded region, but our library of models exhibits relatively little variation of the Hα equivalent width.

seen in most Type II SNe may be particularly relevant to SN GSD11Bus, as that feature intersects the F153M band at redshifts near $z = 1.35$, close to the peak of the GSD11Bus host photo-z distribution. Figure 20 shows that our template library has a marked lack of diversity in Hα flux relative to the integrated flux through the encompassing broad band. Direct observations have shown a much wider range of diversity in the strength and shape of the Hα feature (Patat et al. 1994; Gutiérrez et al. 2014), as would be expected for this heterogeneous class. This suggests that the medium-band photometry for SN GSD11Bus could lead to a more definitive classification and redshift if we had a better set of CC SN templates that more accurately represents the true diversity of these SN types.

<div align="center">REFERENCES</div>

Alard, C., & Lupton, R. H. 1998, ApJ, 503, 325
Amanullah, R., Goobar, A., Clément, B., et al. 2011, ApJ, 742, L7
Arnouts, S., Cristiani, S., Moscardini, L., et al. 1999, MNRAS, 310, 540
Baron, E., Nugent, P. E., Branch, D., & Hauschildt, P. H. 2004, ApJ, 616, L91
Benítez, N. 2000, ApJ, 536, 571
Bertin, E., & Arnouts, S. 1996, A&AS, 117, 393
Betoule, M., Kessler, R., Guy, J., et al. 2014, A&A, 568, A22
Bruzual, G., & Charlot, S. 2003, MNRAS, 344, 1000
Campbell, H., D'Andrea, C. B., Nichol, R. C., et al. 2013, ApJ, 763, 88
Cardelli, J. A., Clayton, G. C., & Mathis, J. S. 1989, ApJ, 345, 245
Chabrier, G. 2003, PASP, 115, 763
Chevallier, M., & Polarski, D. 2001, International Journal of Modern Physics D, 10, 213
Conley, A., Guy, J., Sullivan, M., et al. 2011, ApJS, 192, 1
Contreras, C., Hamuy, M., Phillips, M. M., et al. 2010, AJ, 139, 519
Cowie, L. L., Barger, A. J., Hu, E. M., Capak, P., & Songaila, A. 2004, AJ, 127, 3137
Dahlen, T., Strolger, L.-G., & Riess, A. G. 2008, ApJ, 681, 462
Dahlen, T., Strolger, L.-G., Riess, A. G., et al. 2004, ApJ, 613, 189
Dahlen, T., Mobasher, B., Faber, S. M., et al. 2013, ApJ, 775, 93
Dawson, K. S., Aldering, G., Amanullah, R., et al. 2009, AJ, 138, 1271
Di Carlo, E., Massi, F., Valentini, G., et al. 2002, ApJ, 573, 144
Domínguez, I., Höflich, P., & Straniero, O. 2001, ApJ, 557, 279
Filippenko, A. V. 1997, ARA&A, 35, 309
Folatelli, G., Phillips, M. M., Burns, C. R., et al. 2010, AJ, 139, 120
Foley, R. J., Challis, P. J., Chornock, R., et al. 2013, ApJ, 767, 57
Fontana, A., Dunlop, J. S., Paris, D., et al. 2014, A&A, 570, A11
Frederiksen, T. F., Graur, O., Hjorth, J., Maoz, D., & Poznanski, D. 2014, A&A, 563, A140
Frederiksen, T. F., Hjorth, J., Maund, J. R., et al. 2012, ApJ, 760, 125
Fruchter, A. S., Hack, W., Dencheva, N., Droettboom, M., & Greenfield, P. 2010, in STSCI Calibration Workshop Proceedings,
    Baltimore, MD, 21-23 July 2010, ed. S. D. . C. Oliveira (Space Telescope Science Institute), 376
Ganeshalingam, M., Li, W., & Filippenko, A. V. 2013, MNRAS, 433, 2240
Gilliland, R. L., Nugent, P. E., & Phillips, M. M. 1999, ApJ, 521, 30
Graham, A. W., & Driver, S. P. 2005, PASA, 22, 118
Graur, O., Poznanski, D., Maoz, D., et al. 2011, MNRAS, 417, 916
Graur, O., Rodney, S. A., Maoz, D., et al. 2014, ApJ, 783, 28
Grogin, N. A., Kocevski, D. D., Faber, S. M., et al. 2011, ApJS, 197, 35
Gunnarsson, C., Dahlén, T., Goobar, A., Jönsson, J., & Mörtsell, E. 2006, ApJ, 640, 417
Guo, Q., White, S., Boylan-Kolchin, M., et al. 2011, MNRAS, 413, 101
Guo, Y., Ferguson, H. C., Giavalisco, M., et al. 2013, ApJS, 207, 24
Gutiérrez, C. P., Anderson, J. P., Hamuy, M., et al. 2014, ApJ, 786, L15
Guy, J., Sullivan, M., Conley, A., et al. 2010, A&A, 523, A7
Hemmati, S., Miller, S. H., Mobasher, B., et al. 2014, ApJ, 797, 108
Hernán Caballero, A. 2012, MNRAS, 427, 816
Hicken, M., Challis, P., Jha, S., et al. 2009, ApJ, 700, 331
Hicken, M., Challis, P., Kirshner, R. P., et al. 2012, ApJS, 200, 12
Hildebrandt, H., Arnouts, S., Capak, P., et al. 2010, A&A, 523, A31
Holz, D. E. 1998, ApJ, 506, L1
Holz, D. E., & Linder, E. V. 2005, ApJ, 631, 678
Howell, D. A., Sullivan, M., Conley, A., & Carlberg, R. 2007, ApJ, 667, L37
Hsiao, E. Y., Conley, A., Howell, D. A., et al. 2007, ApJ, 663, 1187
Ilbert, O., Arnouts, S., McCracken, H. J., et al. 2006, A&A, 457, 841
Infante, L. 1987, A&A, 183, 177
Jha, S., Kirshner, R. P., Challis, P., et al. 2006, AJ, 131, 527
Jones, D. O., Rodney, S. A., Riess, A. G., et al. 2013, ApJ, 768, 166
Jönsson, J., Dahlén, T., Goobar, A., et al. 2006, ApJ, 639, 991
Keeton, C. R. 2001, arXiv:astro-ph/0102340
Kessler, R., Becker, A. C., Cinabro, D., et al. 2009a, ApJS, 185, 32
Kessler, R., Bernstein, J. P., Cinabro, D., et al. 2009b, PASP, 121, 1028
Kessler, R., Bassett, B., Belov, P., et al. 2010, PASP, 122, 1415
Kirkpatrick, A., Pope, A., Alexander, D. M., et al. 2012, ApJ, 759, 139
Koekemoer, A. M., Faber, S. M., Ferguson, H. C., et al. 2011, ApJS, 197, 36
Kron, R. G. 1980, ApJS, 43, 305
Laidler, V. G., Papovich, C., Grogin, N. A., et al. 2007, PASP, 119, 1325
Landsman, W. B. 1993, in Astronomical Society of the Pacific Conference Series, Vol. 52, Astronomical Data Analysis Software and
    Systems II, ed. R. J. Hanisch, R. J. V. Brissenden, & J. Barnes, 246
Lidman, C., Howell, D. A., Folatelli, G., et al. 2005, A&A, 430, 843

Linder, E. V. 2003, Physical Review Letters, 90, 091301
Malmquist, K. 1920, Lunds Astron. Obs., Ser, 2, 22
Morokuma, T., Tokita, K., Lidman, C., et al. 2010, PASJ, 62, 19
Murphy, E. J., Chary, R.-R., Alexander, D. M., et al. 2009, ApJ, 698, 1380
Navarro, J. F., Frenk, C. S., & White, S. D. M. 1997, ApJ, 490, 493
O'Donnell, J. E. 1994, ApJ, 422, 158
Patat, F., Barbon, R., Cappellaro, E., & Turatto, M. 1994, A&A, 282, 731
Patel, B., McCully, C., Jha, S. W., et al. 2014, ApJ, 786, 9
Peng, C. Y., Ho, L. C., Impey, C. D., & Rix, H.-W. 2002, AJ, 124, 266
Pickles, A. J. 1998, PASP, 110, 863
Postman, M., Coe, D., Benítez, N., et al. 2012, ApJS, 199, 25
Poznanski, D., Maoz, D., Yasuda, N., et al. 2007, MNRAS, 382, 1169
Rest, A., Scolnic, D., Foley, R. J., et al. 2014, ApJ, 795, 44
Riess, A. G., & Livio, M. 2006, ApJ, 648, 884
Riess, A. G., Filippenko, A. V., Li, W., et al. 1999, AJ, 118, 2675
Riess, A. G., Filippenko, A. V., Liu, M. C., et al. 2000, ApJ, 536, 62
Riess, A. G., Nugent, P. E., Gilliland, R. L., et al. 2001, ApJ, 560, 49
Riess, A. G., Strolger, L.-G., Tonry, J., et al. 2004a, ApJ, 600, L163
—. 2004b, ApJ, 607, 665
Riess, A. G., Strolger, L.-G., Casertano, S., et al. 2007, ApJ, 659, 98
Rodney, S. A., & Tonry, J. L. 2009, ApJ, 707, 1064
Rodney, S. A., Riess, A. G., Dahlen, T., et al. 2012, ApJ, 746, 5
Rodney, S. A., Riess, A. G., Strolger, L.-G., et al. 2014, AJ, 148, 13
Rubin, D., Knop, R. A., Rykoff, E., et al. 2013, ApJ, 763, 35
Sako, M., Bassett, B., Connolly, B., et al. 2011, ApJ, 738, 162
Salzano, V., Rodney, S. A., Sendra, I., et al. 2013, A&A, 557, A64
Scolnic, D., Rest, A., Riess, A., et al. 2014, ApJ, 795, 45
Scolnic, D. M., Riess, A. G., Huber, M. E., et al. 2009, ApJ, 706, 94
Sérsic, J. L. 1963, Boletin de la Asociacion Argentina de Astronomia La Plata Argentina, 6, 41
Stritzinger, M. D., Phillips, M. M., Boldt, L. N., et al. 2011, AJ, 142, 156
Strolger, L.-G., & Riess, A. G. 2006, AJ, 131, 1629
Strolger, L.-G., Riess, A. G., Dahlen, T., et al. 2004, ApJ, 613, 200
Sullivan, M., Le Borgne, D., Pritchet, C. J., et al. 2006, ApJ, 648, 868
Suzuki, N., Rubin, D., Lidman, C., et al. 2012, ApJ, 746, 85
Timmes, F. X., Brown, E. F., & Truran, J. W. 2003, ApJ, 590, L83
Tonry, J. L., Schmidt, B. P., Barris, B., et al. 2003, ApJ, 594, 1
Tripp, R. 1998, A&A, 331, 815
Wirth, G. D., Willmer, C. N. A., Amico, P., et al. 2004, AJ, 127, 3121
Yang, X., Mo, H. J., van den Bosch, F. C., Zhang, Y., & Han, J. 2012, ApJ, 752, 41
Zheng, C., Romani, R. W., Sako, M., et al. 2008, AJ, 135, 1766